

1

Snow Interception Relationships with 2 Meteorology and Canopy Density in a 3 Subalpine Forest

4

5 **Authors:**

6 Alexander Charles Cebulski¹ (ORCID ID - 0000-0001-7910-5056)

7 John Willard Pomeroy¹ (ORCID ID - 0000-0002-4782-7457)

8 ¹Centre for Hydrology, University of Saskatchewan, Canmore, Canada

9 **Corresponding Author:** A.C. Cebulski, 50 Lincoln Park, Canmore, Alberta, Canada, T1W

10 3E9, alex.cebulski@usask.ca

11 **Abstract:** Snow accumulation models differ in how snow interception and ablation processes
12 are represented and thus their application to diverse climates and forest types is uncertain.
13 Existing parameterizations of initial snow interception before unloading include inherently cou-
14 pled canopy snow accumulation and ablation processes. This leads to difficulty in diagnosing
15 processes and adding possible errors to simulations when incorporated as canopy interception
16 routines in models that already account for canopy snow ablation. This study evaluates the
17 theory underpinning parameterizations of initial snow interception using high-temporal reso-
18 lution and fine-scale measurements of throughfall for events with minimal snow ablation and
19 redistribution in both the canopy and on the ground. The relationship between these through-
20 fall measurements, event meteorology, and a novel lidar-based canopy density measurement

21 are assessed in two subalpine forest plots in the Canadian Rockies. Contrary to existing the-
22 ories, no association of canopy snow load or air temperature with interception efficiency was
23 observed. Instead, canopy density emerged as the primary factor governing snow accumula-
24 tion. A wind-driven snowfall event demonstrated that non-vertical hydrometeor trajectories
25 can significantly increase snow-leaf contact area, thereby enhancing initial interception before
26 ablation. Prediction of interception efficiency for this event improved dramatically when ad-
27 justed for hydrometeor trajectory angle based on a wind speed at one-third of the canopy
28 height. Snow-leaf contact area showed a high sensitivity to wind speed, increasing by up
29 to 95% with a 1 m s^{-1} wind speed. The study proposes a new parameterization that calcu-
30 lates throughfall, independent of processes that ablate snow from the canopy, as a function
31 of snowfall, canopy cover, and wind speed. This new parameterization successfully estimated
32 subcanopy snow accumulation for a snowfall event at two forest plots measured using lidar and
33 snow surveys. By separating canopy snow ablation from snow interception processes, this new
34 model offers potentially improved prediction of subcanopy snow accumulation when combined
35 with canopy snow ablation parameterizations.

36 **Keywords:** snow interception, throughfall, ablation, forest, snowpack, lidar, process-based
37 modelling

38 1 Introduction

39 Over half of North America's snow-covered zone is covered by forests (Kim et al., 2017), signif-
40 icantly impacting the accumulation and redistribution of snowpacks and subsequent snowmelt
41 runoff. Essery et al. (2003) estimated that 25–45% of annual snowfall may be lost to the atmo-
42 sphere due to sublimation of snow intercepted in forest canopies globally. Snow intercepted in
43 the canopy can sublimate and melt at much higher rates than the subcanopy snowpack (Kat-
44 sushima et al., 2023; Lundberg & Hallidin, 1994; Pomeroy et al., 1998), reducing the amount
45 of snow available for runoff. Canopy density is one of the primary factors controlling the parti-
46 tioning of snowfall into throughfall and interception (Hedstrom & Pomeroy, 1998; Storck et al.,

47 2002), and thus governs the quantity of snow subject to sublimation from the canopy. However,
48 forest thinning efforts aimed at limiting sublimation losses to increase snowmelt runoff do not
49 always lead to a corresponding increase in spring streamflow (Golding & Swanson, 1978; Har-
50 pold et al., 2020; Pomeroy et al., 2012; Troendle, 1983). This may be due to increased ablation
51 rates when forest cover is reduced, desynchronization of snowmelt, and sub-surface hydrology
52 interactions (Ellis et al., 2013; Musselman et al., 2015; Pomeroy et al., 1997; Safa et al., 2021;
53 Varhola et al., 2010). Given the significant impact of forest cover on snowpacks, along with the
54 limited or absent monitoring networks for subcanopy snow accumulation (Rittger et al., 2020;
55 Vionnet et al., 2021), land management, ecological conservation, and water resource decisions
56 depend on reliable models of snow redistribution.

57 Hedstrom & Pomeroy (1998), working in the cold continental boreal forest, proposed that
58 initial snow interception efficiency was controlled by the maximum canopy load which itself
59 was a function of leaf area index and new snow density. Unloading was found to be an ex-
60 ponential function of time that was observed only days or weeks after the interception event.
61 Storck et al. (2002), working in temperate coastal forests, emphasized the role of leaf area
62 index and air temperature in controlling the maximum canopy snow load. Gelfan et al. (2004)
63 demonstrated accurate subcanopy snowpack simulations at study sites in Russia by treating
64 the Hedstrom & Pomeroy (1998) and Storck et al. (2002) parameterizations separately while
65 using a step-based function to choose either parameterization based on air temperature. A
66 similar parameterization in the Cold Regions Hydrological Model (Pomeroy et al., 2022) has
67 shown strong performance at sites across Canada, northern United States, Switzerland, and
68 Spain. However, overestimation of subcanopy snow accumulation was reported by Lundquist
69 et al. (2021) and Lumbrazo et al. (2022) when combining the Hedstrom & Pomeroy (1998)
70 routine with ablation parameterizations from different studies (e.g., Roesch et al., 2001). The
71 coupling of ablation processes within existing snow interception models (Hedstrom & Pomeroy,
72 1998; Storck et al., 2002) may contribute to overestimates of throughfall, canopy snow unload-
73 ing, and canopy snow melt when combined with other canopy snow ablation parameterizations
74 (Cebulski & Pomeroy, 2025). Additional observations of snow interception that exclude abla-

tion processes could help determine the applicability of the interception theories proposed by Hedstrom & Pomeroy (1998) and Storck et al. (2002). Hedstrom & Pomeroy's (1998) theory also suggests that moderate wind speeds, which can result in more horizontal hydrometeor trajectories, increasing snow-leaf contact area and interception efficiency at the plot scale. This association has also been shown in rainfall interception studies to decrease throughfall of rain (Herwitz & Slye, 1995; Van Stan et al., 2011). However, the relationship proposed by Hedstrom & Pomeroy (1998), is typically not included in snow accumulation models as empirical testing of this relationship is lacking.

The objective of this paper is to evaluate the theories underlying existing snow interception models using high spatial and temporal resolution measurements of subcanopy snow accumulation for events with minimal canopy snow ablation. These new observations are investigated to address the following research questions:

1. Are the existing theories regarding the relationships between meteorology and canopy density and initial snow interception supported by in-situ observations collected in the Canadian Rockies?
2. Is snow interception influenced by non-vertical hydrometeor trajectory angles over a wind-driven snowfall event?
3. To what extent can these findings inform the development of a new parameterization for snow interception?

2 Theory

2.1 Canopy snow mass balance

The change in canopy snow load over time, $\frac{dL}{dt}$ (mm s⁻¹), can be estimated from the mass balance:

$$\frac{dL}{dt} = [q_{sf} - q_{tf} + q_{ros}] - q_{unld} - q_{drip} - q_{wind}^{veg} - q_{sub}^{veg} \quad (1)$$

where q_{sf} is the snowfall rate (mm s^{-1}), q_{ros} (mm s^{-1}) is the rate of rainfall falling on snow intercepted in the canopy, q_{tf} (mm s^{-1}) is the throughfall rate (mm s^{-1}), q_{unld} is the canopy snow unloading rate (mm s^{-1}), q_{drip} is the canopy snow drip rate due to canopy snowmelt (mm s^{-1}), q_{wind}^{veg} is the wind transport rate in or out of the control volume (mm s^{-1}), and q_{sub}^{veg} is the intercepted snow sublimation rate (mm s^{-1}). Figure 1 in Cebulski & Pomeroy (2025) presents a visual representation of this mass balance.

Interception efficiency, $\frac{I}{P}$ (-), which is the fraction of snowfall intercepted over Δt before ablation, can be calculated as:

$$\frac{I}{P} = \frac{\Delta L}{q_{sf}\Delta t} \quad (2)$$

During periods with low air temperatures and low wind speeds, q_{ros} , q_{unld} , q_{drip} , q_{wind}^{veg} , and q_{sub}^{veg} can be assumed negligible and thus the right side of Equation 1 can be simplified and used as an approximation of ΔL to calculate $\frac{I}{P}$ as:

$$\frac{I}{P} = \frac{(q_{sf} - q_{tf})\Delta t}{q_{sf}\Delta t} \quad (3)$$

2.2 Hydrometeor trajectory angle

Herwitz & Slye (1995) calculate the trajectory angle of a hydrometeor, θ_h , as the departure in degrees ($^\circ$) from a vertical plane as:

$$\theta_h = \arctan \left(\frac{x_h(u_z)}{v_h(D_h)} \right) * \frac{180}{\pi} \quad (4)$$

112 where $v_h(D_h)$ is the terminal fall velocity of the hydrometeor (m s^{-1}), which is a function of
113 the hydrometeor diameter, D_h and $x_h(u_z)$ is the horizontal velocity of the hydrometeor (m
114 s^{-1}) which is a function of the within canopy wind speed, u_z at height above ground, z . In the
115 absence of hydrometeor velocity observations, $v_h(D_h)$ may be approximated from values in the
116 literature (e.g., 0.8 m s^{-1} in Isyumov (1971)) and $x_h(u_z)$ can be approximated by the horizontal
117 wind speed. This assumes the hydrometeors are following fluid points in the atmosphere.

118 **2.3 Within-canopy wind flow**

119 Cionco (1965) show that, u_z may be approximated using the exponential formula:

$$120 u_z = u \cdot \exp \left[a \cdot \left(\frac{z}{h_c} - 1 \right) \right] \quad (5)$$

121 where u is the horizontal wind speed at the top of the canopy (m s^{-1}), a is an attenuation
122 coefficient, z is the height above ground (m), and h_c is the average height of the canopy
123 elements. Parviaainen & Pomeroy (2000) provided a method to calculate a using observations
from two jack pine stands, which was applied in this study.

124 **3 Data and methods**

125 **3.1 Study site**

126 This study was conducted at Fortress Mountain Research Basin (FMRB), Alberta, Canada,
127 -115° W , 51° N , a continental headwater basin in the Canadian Rockies (Figure 1). Data
128 from this study was collected between October 2021 and July 2023 within and surrounding
129 two forest plots adjacent to the FMRB Powerline Station (PWL) and Forest Tower Station
130 (FT) at $\sim 2100 \text{ m}$ above sea level as shown in Figure 1. The average annual precipitation at
131 PWL Station from 2013 to 2023 was 1045 mm, with the peak annual snow water equivalent
132 (SWE) reaching 465 mm, typically occurring in late April. The PWL plot is adjacent to PWL

¹³³ station and the FT plot surrounds FT station and both include discontinuous stands of 70%
¹³⁴ subalpine fir (*Abies lasiocarpa*) and 30% Engelmann spruce (*Picea engelmannii*) (Langs et al.,
¹³⁵ 2020). The canopy closure of the two forest plots are 0.51 and 0.29 and the winter leaf area
¹³⁶ indices are 2.07 and 1.66 for PWL and FT respectively. The average height of the canopy
¹³⁷ within the PWL plot is 10.5 m and within the FT plot is 7.1 m. In August of 1936, the
¹³⁸ majority of vegetation in FMRB burned during a large forest fire that affected most of the
¹³⁹ Kananaskis Valley (Fryer et al., 1988). Following the fire, the forest within the PWL and FT
¹⁴⁰ forest plots has naturally regenerated, though some trees have been removed for road clearing
¹⁴¹ and creation of a snow study plot.

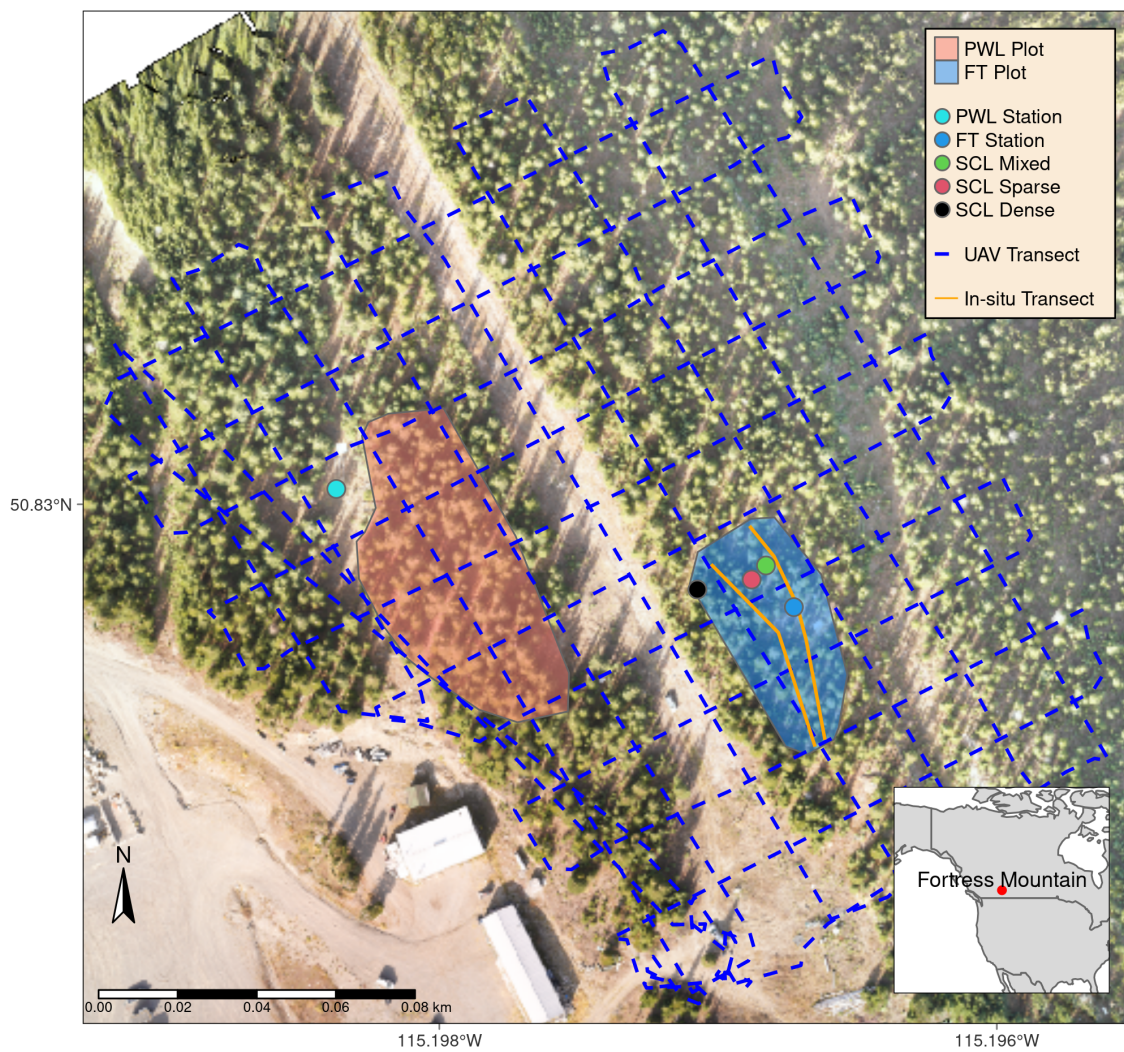


Figure 1: Map showing the location of forest plots, flux towers, subcanopy lysimeter instruments (SCL), and survey transects. The inset map on the lower right shows the regional location of Fortress Mountain Research basin.

¹⁴² **3.2 Meteorological measurements**

¹⁴³ Measurements of air temperature and relative humidity (Vaisala model HMP155A), wind speed
¹⁴⁴ and direction (RM Young model 86000 2-D ultrasonic anemometer) were made 4.3 m above
¹⁴⁵ the ground at FT station (Figure 1). Wind speed measurements from a 3-cup anemometer
¹⁴⁶ (Met One model 014A), installed adjacent to the 2-D ultrasonic anemometer at 4.3 m, were
¹⁴⁷ used to fill data gaps in the 2-D ultrasonic anemometer records.

¹⁴⁸ At PWL station, the snowfall rate was measured by an Alter-shielded OTT Pluvio weighing
¹⁴⁹ precipitation gauge 2.6 m above ground, corrected for undercatch following phase correction
¹⁵⁰ by Harder & Pomeroy (2013) and catch efficiency by Smith (2007). The instrument accuracy
¹⁵¹ of the OTT Pluvio specified in the instrument manual is +/- 0.1 mm or 0.2% (whichever is
¹⁵² larger). Wind speed for undercatch correction was measured by a 3-cup anemometer (Met One
¹⁵³ model 014A) at a height of 2.6 m at PWL station. An optical disdrometer (OTT Parsivel2)
¹⁵⁴ provided measurements of hydrometeor particle size and vertical velocity. All measurements
¹⁵⁵ were recorded at 15-min intervals using Campbell Scientific dataloggers, except the Parsivel2
¹⁵⁶ which was recorded at 1-minute intervals by an onsite computer.

¹⁵⁷ **3.3 Lysimeter measurements**

¹⁵⁸ Three subcanopy lysimeters (SCLs) were installed surrounding the FT Station (Figure 1) to
¹⁵⁹ provide measurements of throughfall as in MacDonald (2010). Figure 2 shows the three SCLs
¹⁶⁰ which consisted of a plastic horse-watering trough with an opening of 0.9 m² and depth of 20
¹⁶¹ cm suspended from a load cell (Intertechnology 9363-D3-75-20T1) attached to an aluminum
¹⁶² pipe connected between two trees. For 26 distinct snowfall events, where canopy snow ablation
¹⁶³ rates were deemed negligible, snow captured in the SCLs was determined to be predominantly
¹⁶⁴ from throughfall. Timelapse imagery, mass change on a weighed tree lysimeter “hanging tree”
¹⁶⁵ (Pomeroy & Schmidt, 1993), and in-situ observations were used to ensure unloading, melt,
¹⁶⁶ and wind redistribution of canopy snow was minimal over each interval. Additionally, the
¹⁶⁷ throughfall measurements were filtered to include observations that coincided with a snowfall

168 rate > 0 mm hr⁻¹ and a snowfall rate that exceeded the SCL measured throughfall rate. While
169 these careful manual mitigation and automated filtering strategies substantially reduce the
170 contribution of unloading in the SCL throughfall measurements, a small contribution is still
171 possible.

172 The SCL throughfall measurements were converted from weight, to weight per unit area by
173 dividing the snow weight in the SCL by the cross-sectional area of the SCL opening. Canopy
174 snow load was also estimated using Equation 1, incorporating throughfall measurements from
175 the SCLs and snowfall measurements from the PWL gauge. The manufacturer-specified com-
176 bined error of full scale output for the load cells is +/- 0.02% with a temperature sensitivity
177 of +/- 0.001%/5°C. The small amount of snow captured in the SCLs and Pluvio instruments
178 over the 15-minute intervals led to very high relative instrument errors. To reduce this error,
179 throughfall and snowfall measurements were accumulated. While suitable instrument errors
180 were found for longer time intervals (greater than 12 hours), at these intervals, the relation-
181 ship between interception efficiency and meteorological measurements became non-stationary.
182 Therefore, to ensure consistency between throughfall and snowfall measurements and meteoro-
183 logical conditions, air temperature, wind speed, and initial canopy snow load (measured from
184 the weighed tree) were binned. Snowfall and throughfall measurements were then accumu-
185 lated within each bin. Interception efficiency was subsequently calculated for each bin using
186 Equation 3 and the accumulated measurements of snowfall and throughfall.

187 The SCLs were installed in locations selected to limit preferential throughfall and unloading
188 by choosing locations with relatively continuous spatial distribution of canopy elements (i.e.,
189 canopy structure) and away from large branches which could preferentially unload snow. The
190 “mixed” canopy SCL had a slight canopy opening, shown in Figure 2, orientated towards the
191 prevailing wind direction observed during the study period which allowed some preferential
192 measurement of throughfall for snowfall trajectories aligned with this gap. The canopy sur-
193 rounding the SCLs led to reduced wind speeds and reduced the potential for gauge undercatch
194 by the SCLs. Photographs of the three SCLs and surrounding canopy are shown in Figure 2.
195 Leaf area index and canopy closure measurements of canopy density for each SCL are pre-

sented in Table 1. A viewing angle of 60° from zenith was selected to describe the SCLs in the results section as non vertical hydrometeor trajectory angles were expected to influence the measurements at these locations. The canopy density metrics were measured using hemispherical photography (Nikon Coolpix 4500 and EC-F8 hemispherical lens) and analyzed with the hemispheR R package Chianucci & Macek (2023).

The weighed tree lysimeter, a live subalpine fir (*Abies lasiocarpa*) tree suspended from a load cell (Artech S-Type 20210-100) measured the weight of canopy snow load (kg). This weight was scaled to an areal estimate of canopy snow load (L , mm) using measurements of areal throughfall (mm) from in-situ snow surveys and snowfall from the PWL Station snowfall gauge following the method in Pomeroy & Schmidt (1993). Although the weighed tree lysimeter provides a more direct measurement of canopy snow load compared to the SCLs, it was not used in the interception efficiency calculation as variations in the trees mass may be attributed to canopy snow sublimation, unloading and melt. Since the subcanopy lysimeter estimates of canopy snow load are not influenced by sublimation, they provided a measurement of interception efficiency with less uncertainty.

Table 1: Canopy density of the three subcanopy lysimeters (SCL) located proximal to the FT Station. Leaf area index (LAI) and canopy closure was measured using hemispherical photo analysis for varying viewing angles from zenith.

Name	Angle From Zenith (°)	LAI (-)	Canopy Closure (-)
Sparse	15	0.45	0.19
Sparse	30	1.12	0.44
Closed	15	1.58	0.54
Sparse	45	1.43	0.56
Mixed	15	2.00	0.63
Sparse	60	1.56	0.64
Closed	30	2.01	0.65
Mixed	30	2.34	0.71
Mixed	45	2.33	0.74

Table 1: Canopy density of the three subcanopy lysimeters (SCL) located proximal to the FT Station. Leaf area index (LAI) and canopy closure was measured using hemispherical photo analysis for varying viewing angles from zenith.

Name	Angle From Zenith (°)	LAI (-)	Canopy Closure (-)
Mixed	60	2.10	0.75
Closed	45	2.47	0.76
Closed	60	2.40	0.79

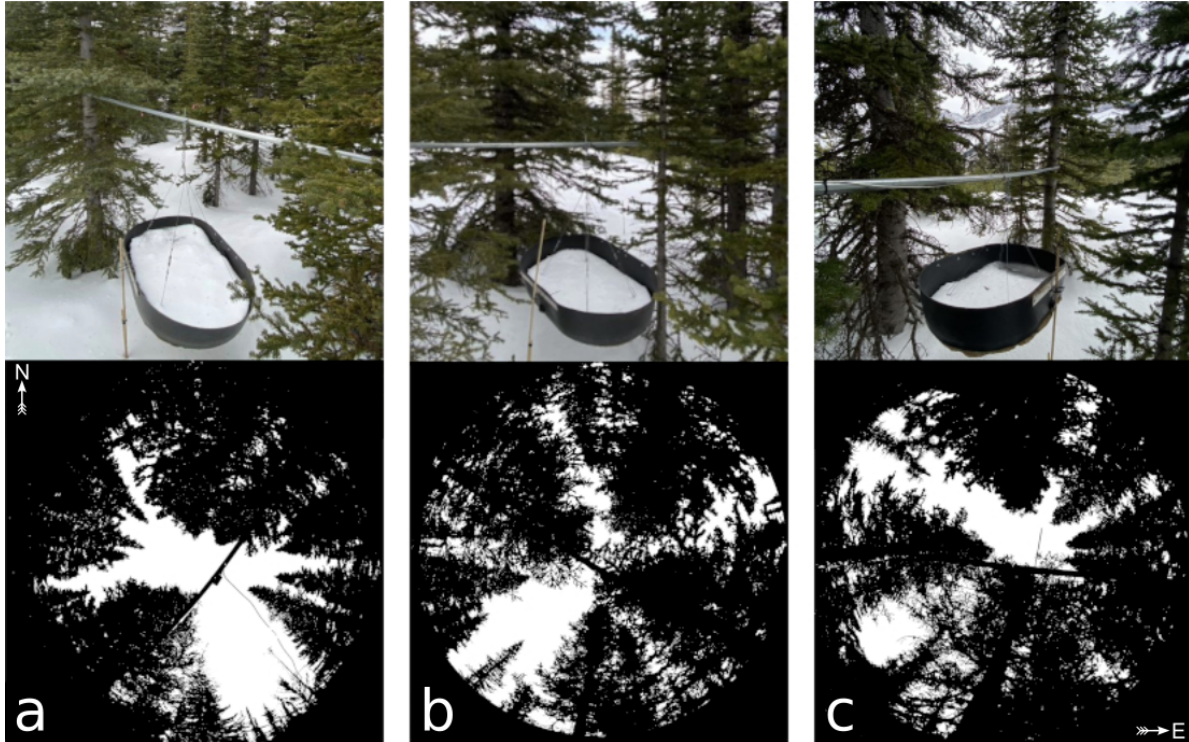


Figure 2: Images of the three subcanopy lysimeters (SCL) and surrounding canopy located in sparse (a), mixed (b), and dense (c) canopy. The top row presents a side view of each SCL and the bottom row shows hemispherical photographs classified using the hemispheR R package. These hemispherical images are oriented with north at the top and have been mirrored to provide a view from above (e.g., east is on the right side of each image). See Table 1 for the canopy density measurements above each SCL.

211 3.4 UAV-Lidar data collection and processing

212 The UAV (FreeFly Alta X) payload included a REIGL miniVUX-2 airborne laser scanner,
213 an Applanix APX-20 inertial measurement unit (IMU) and global navigation satellite system
214 (GNSS). The UAV was flown 90 m above the ground at a speed of 3 m s^{-1} following the path
215 shown in Figure 1. The methods outlined by Harder et al. (2020) and Staines & Pomeroy
216 (2023) were incorporated to reconcile survey lidar, IMU and GNSS data. A systematic vertical
217 bias of up to 6 cm between UAV-lidar flight lines was observed in the resulting point clouds
218 on March 13th and 14th, 2024 and was attributed to IMU position drift. After strip alignment,
219 the mean elevation bias in the point clouds compared to the GNSS data was 0.000 m and the
220 RMS error declined from 0.055 m to 0.038 m on March 13th and changed from 0.033 m to
221 0.029 m on March 14th. The point cloud density ranged from ~1200 returns m^2 in sparse forest
222 to ~2200 returns m^2 in open clearings. Quality control, ground classification, calculation of
223 surface elevation change was conducted on the point cloud data and then converted to 0.05 m
224 resolution rasters. Further quality control was conducted on the 0.05 m raster data to remove
225 values that exceeded the .999th quantile and then resampled to 0.25 m grid cell resolution by
226 taking the median. A detailed description of the UAV, payload, flight settings, and software
227 packages used is provided in the supporting information.

228 3.5 Snow surveys

229 3.5.1 In-situ snow depth and density

230 Event-based snow surveys provided measurements of subcanopy throughfall depth and density
231 at 30 locations following the transects shown in Figure 1. These measurements were used
232 to upscale the weighed tree from weight to weight per unit area, assess the accuracy of lidar
233 derived snow depth measurements, and provide a fresh snow density for the calculation of SWE
234 (mm) from the snow depth measurements. Minimal ablation and redistribution of both the
235 surface snowpack and/or snow intercepted in the canopy was crucial to ensure the snow survey

measurements were attributed to throughfall. Therefore, only snowfall events with minimal canopy snow ablation as determined through in-situ observations, analysis of timelapse imagery, and mass change on the weighed tree lysimeter were selected. A 1000 cm³ Perla snow density wedge sampler (RIP Cutter, <https://snowmetrics.com/shop/rip-1-cutter-1000-cc/>) was used to measure the density of the fresh snow layer, $\bar{\rho}_{tf}$ (kg m⁻³) from snow pits. Throughfall depth measurements, ΔHS were converted to SWE using the following equation:

$$\Delta SWE_{tf} = \Delta HS \cdot \bar{\rho}_{tf} \quad (6)$$

If a pre-event crust layer was present, the depth of post event fresh snow accumulation above the crust layer was interpreted as throughfall over the event. In the absence of a defined crust layer, the difference in pre- and post-event snow depth to ground was interpreted as event throughfall.

3.5.2 UAV-Lidar snow depth

Two uncrewed aerial vehicle (UAV) lidar surveys were conducted before and after a 24-hour snowfall event that occurred between March 13–14th, 2023 to facilitate the measurement of snow accumulation and canopy density within the FT and PWL forest plots. This period was selected based on two criteria: 1) it provided sufficient cumulative snowfall to result in a low relative error in UAV-lidar measured throughfall, and 2) minimal snow redistribution and ablation was observed, as confirmed by the SCLs, weighed tree, and time-lapse imagery. The change in surface elevation between the two UAV-lidar point clouds was interpreted as the increase in snow accumulation, ΔHS , over the snowfall event. ΔSWE_{tf} was calculated using Equation 6 together with in-situ measurements of $\bar{\rho}_{tf}$. The measurement error of the UAV-lidar derived ΔHS was assessed using the in-situ snow depth observations which is shown in the supporting information. Spatially distributed measurements of $\frac{I}{P}$, were then determined using Equation 3 by using ΔSWE_{tf} as the throughfall component ($q_{tf}\Delta t$) and the snowfall accumulation to the open ($q_{sf}\Delta t$) measured between the two lidar surveys at PWL station.

260 **3.6 UAV-Lidar canopy metrics**

261 The canopy of the study site was characterized from two UAV-lidar point clouds (March 13th
262 and March 14th) using the voxel ray sampling (VoxRS) methodology for lidar data analysis,
263 as developed by Staines & Pomeroy (2023). This method was chosen for its ability to provide
264 canopy metrics that are less sensitive to the inherent non-uniform nature of lidar sampling data,
265 which often results from beam occlusion in vegetation and leads to reduced points near the
266 ground. Using this method radiation transmittance, τ (-), was measured across the hemisphere
267 at a 1° step, e.g., azimuth angles (0°, 1°, ..., 359°) and zenith angles (0°, 1°, ..., 90°) for each
268 0.25 m grid cell within the FT and PWL forest plots. The fraction of snow-leaf contact area
269 per unit area of ground proposed by Hedstrom & Pomeroy (1998), and hereafter called leaf
270 contact area (C_p), was then calculated as:

$$C_p(C_c, \theta_h, L) = 1 - \tau \quad (7)$$

$$C_p(C_c, \theta_h, L) = \begin{cases} 1 - \tau, & \text{if } \theta_h > 0^\circ \\ 1 - \tau \approx C_c, & \theta_h = 0^\circ \end{cases} \quad (8)$$

271 where C_p is a function of the canopy cover C_c , hydrometeor trajectory angle (θ_h), and canopy
272 snow load (L). C_c is the fraction of canopy area to total ground area when viewed from above,
273 which differs from canopy closure, an angular-derived metric usually measured from the ground
274 perspective.

275 To determine how C_p was associated with interception efficiency at different azimuth and zenith
276 angles over the March 13–14th snowfall event, the entire hemisphere at each grid location was
277 considered. The relationship between interception efficiency and C_p was found to be linear
278 and thus the Pearson Correlation Coefficient (ρ_p) was used. The ρ_p was computed between a
279 single raster of interception efficiency and each of the 32,760 rasters of C_p measured on March

280 13th, representing locations across the hemisphere (azimuth [0°, 1°, ..., 359°], zenith angle [0°,
281 1°, ..., 90°]) at 0.25 m grid cells spanning the FT and PWL forest plots.

282 **3.7 Statistics and regression models**

283 Linear and non-linear regression models were developed to assess relationships in the observed
284 data. Linear models were fitted using ordinary least squares regression to analyze two re-
285 lationships: (1) between interception efficiency and meteorological variables and (2) between
286 interception efficiency and leaf contact area. The latter was forced through the origin based on
287 the theoretical justification that the dependent variable should be zero when the independent
288 variable is zero. Kozak & Kozak (1995) noted, the default R^2 value provided for least squares
289 models forced through the origin by many statistical packages can be misleading. Therefore,
290 these R^2 values were adjusted using Equation 10 in Kozak & Kozak (1995). Non-linear models
291 were fitted to investigate the relationship of leaf contact area with simulated trajectory angle
292 using non-linear least squares regression. All statistical analyses were conducted using the R
293 ‘stats’ package (R Core Team, 2024).

294 **4 Results**

295 **4.1 The influence of meteorology on snow interception**

296 Figure 3 shows that canopy snow load increases linearly with cumulative snowfall, with no
297 evidence of reaching a maximum, across 26 snowfall events for both the SCL and weighed tree
298 measurements. Over these events, air temperature ranged from -24.5°C to 1°C, wind speeds at
299 4.3 m height ranged from calm to 4.6 m s⁻¹ (Table 2), and wind direction was predominately
300 from the southwest during snowfall (Figure 4). Missing canopy snow load measurements, as
301 shown in Figure 3 for certain events, were caused by wiring damage from animals and heavy
302 snow loads. Some of the the variability in interception rates within and between different
303 events may be attributed to small amounts of canopy snow unloading and melt, which could

not be fully accounted for through the manual and automated filtering mitigation strategies for in both the SCL and weighed tree measurements. Additionally, the weighed tree lysimeter was influenced by canopy snow sublimation, which was not directly accounted for in our analysis.

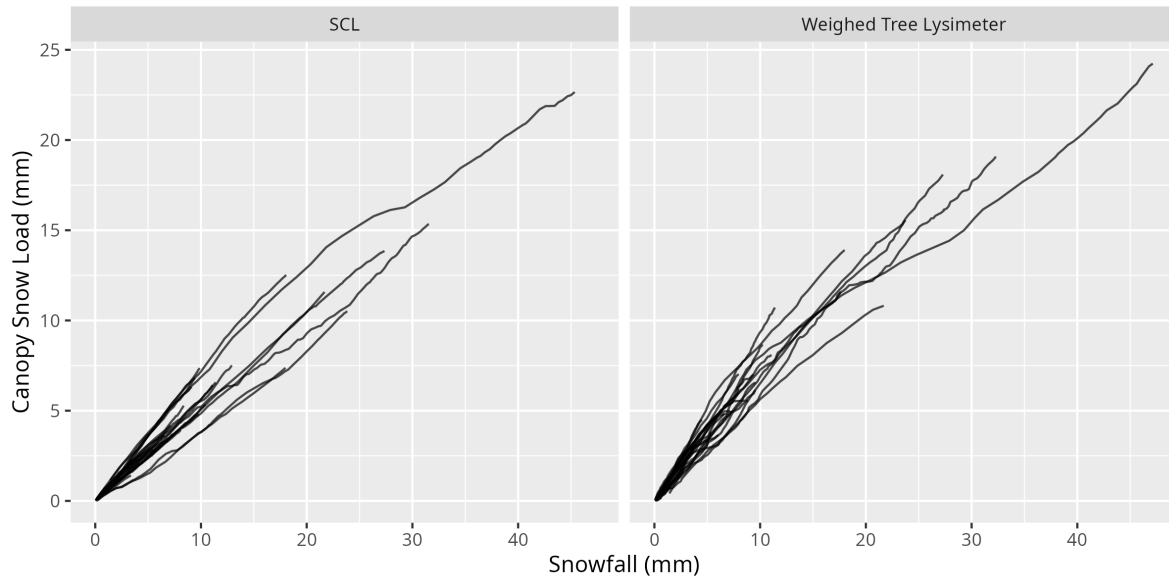


Figure 3: Plot showing the cumulative event snowfall versus the corresponding state of canopy snow load calculated using the average of the three subcanopy lysimeters (SCL, left) and weighed tree lysimeter (right) for each of the 26 snowfall events.

Table 2: Meteorology of the 26 snowfall events. Air temperature and wind speed were measured at FT station. Interception efficiency is estimated from snowfall measured at PWL station and the average throughfall of all three SCLs located within the FT forest plot (all from 15-min. measurements).

Start Date	Air Temperature (°C)			Wind Speed (m/s)			Interception Efficiency (-)			Snowfall (mm)
	Min	Mean	Max	Min	Mean	Max	Min	Mean	Max	
2021-12-23	-6.2	-5.3	-4.6	0.6	3.1	4.6	0.1	0.5	0.9	21.7
2022-01-02	-15.9	-10.8	-5.8	0.2	1.8	4.2	0.0	0.5	1.0	31.6
2022-01-17	-14.8	-7.8	-0.8	0.2	1.1	1.8	0.0	0.6	1.0	12.9
2022-01-31	-24.5	-12.1	-6.4	0.1	1.0	1.7	0.2	0.7	1.0	9.1
2022-02-14	-9.9	-9.0	-8.5	0.4	0.8	1.2	0.2	0.5	0.8	1.7
2022-02-19	-4.7	-3.2	-2.5	1.3	2.3	3.6	0.3	0.6	0.9	11.1
2022-03-01	-8.3	-5.4	-1.0	0.1	1.0	3.1	0.4	0.8	1.0	9.9
2022-03-07	-12.5	-8.6	-4.4	0.3	0.8	1.7	0.3	0.7	1.0	9.5
2022-03-14	-2.7	-2.1	-0.8	1.0	1.6	2.9	0.2	0.6	0.9	8.4
2022-03-19	-3.1	-2.8	-2.5	0.0	0.7	1.3	0.3	0.5	0.6	6.6
2022-03-23	-7.9	-5.3	-0.9	0.8	1.2	1.8	0.4	0.6	0.9	1.6
2022-04-04	-3.5	-2.9	-2.1	0.6	1.0	1.9	0.0	0.4	0.6	3.4
2022-04-18	-5.2	-4.0	-2.7	0.4	1.1	1.9	0.1	0.5	0.9	7.4
2022-04-22	-2.8	-1.8	-0.5	0.4	0.8	1.2	0.1	0.5	1.0	9.8
2022-05-09	-4.9	-4.3	-3.2	0.1	0.4	0.9	0.2	0.5	0.9	8.1
2022-05-19	-4.9	-2.1	0.3	0.1	0.4	0.9	0.2	0.6	0.9	7.1
2022-06-13	-1.1	-0.3	0.6	0.1	0.1	0.4	0.0	0.5	0.9	45.4
2022-12-27	-3.0	-2.7	-1.9	0.6	1.1	1.8	0.2	0.5	0.9	4.5
2023-01-27	-11.5	-7.3	-4.5	0.6	0.9	1.2	0.1	0.5	0.8	10.4
2023-02-19	-14.3	-9.5	-6.3	0.2	0.8	1.4	0.2	0.7	1.0	18.1
2023-02-26	-9.2	-8.4	-6.6	0.2	1.0	2.1	0.3	0.5	1.0	5.4
2023-03-13	-8.9	-3.6	-0.1	0.3	1.3	2.2	0.0	0.5	1.0	27.4
2023-03-24	-7.9	-5.7	-3.5	0.1	0.5	1.2	0.1	0.4	0.7	23.8
2023-04-01	-8.9	-7.7	-4.7	0.1	0.6	1.4	0.4	0.6	0.8	11.4
2023-04-10	-1.1	-0.5	0.3	0.1	0.3	1.0	0.2	0.4	0.6	18.0
2023-05-08	0.2	0.6	1.0	0.4	0.6	0.8	0.6	0.6	0.7	3.5

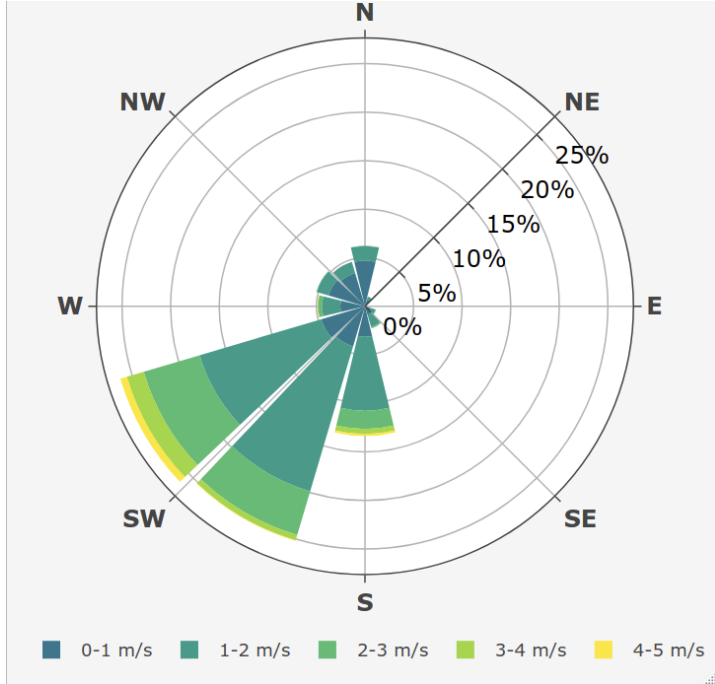


Figure 4: Wind rose showing the frequency of wind speed and direction over the 26 snowfall periods for the ultrasonic anemometer 4.3 m above ground at FT station.

Figure 5 shows interception efficiency calculated from accumulated snowfall (Pluvio) and throughfall (SCL) measurements for bins of air temperature, wind speed, and initial canopy snow load for periods with minimal canopy snow ablation. Accumulated snowfall ranged from 2–107 mm and accumulated throughfall ranged from 0.6–47 mm across the differing bins. The absolute instrument error within each bin ranged from $+/-0.01\text{--}0.02$ mm for the throughfall measurements and from $+/-1.70\text{--}2.60$ mm for the snowfall measurements. The interception efficiency observed across differing bins of air temperature does not show any systematic trend (Figure 5). While air temperature bins below -10°C show slightly higher interception efficiency for the sparse and mixed canopies, the high uncertainty of these interception efficiency measurements, make any potential trend with air temperature highly uncertain. An increasing trend in interception efficiency with increasing wind speed was observed for the sparse and closed canopies (Figure 6b). Although interception efficiency continues increasing for wind speeds above 2 m s^{-1} , the high uncertainty in these interception efficiencies limits this trend

320 to below 2 m s^{-1} . A small increase in interception efficiency is observed for the sparse and
321 closed canopies when the snow load is less than 7 mm (Figure 6c). Interception efficiency later
322 declined for snow loads greater than 7 mm for all three canopies before the uncertainty in the
323 interception efficiency measurements becomes substantial.

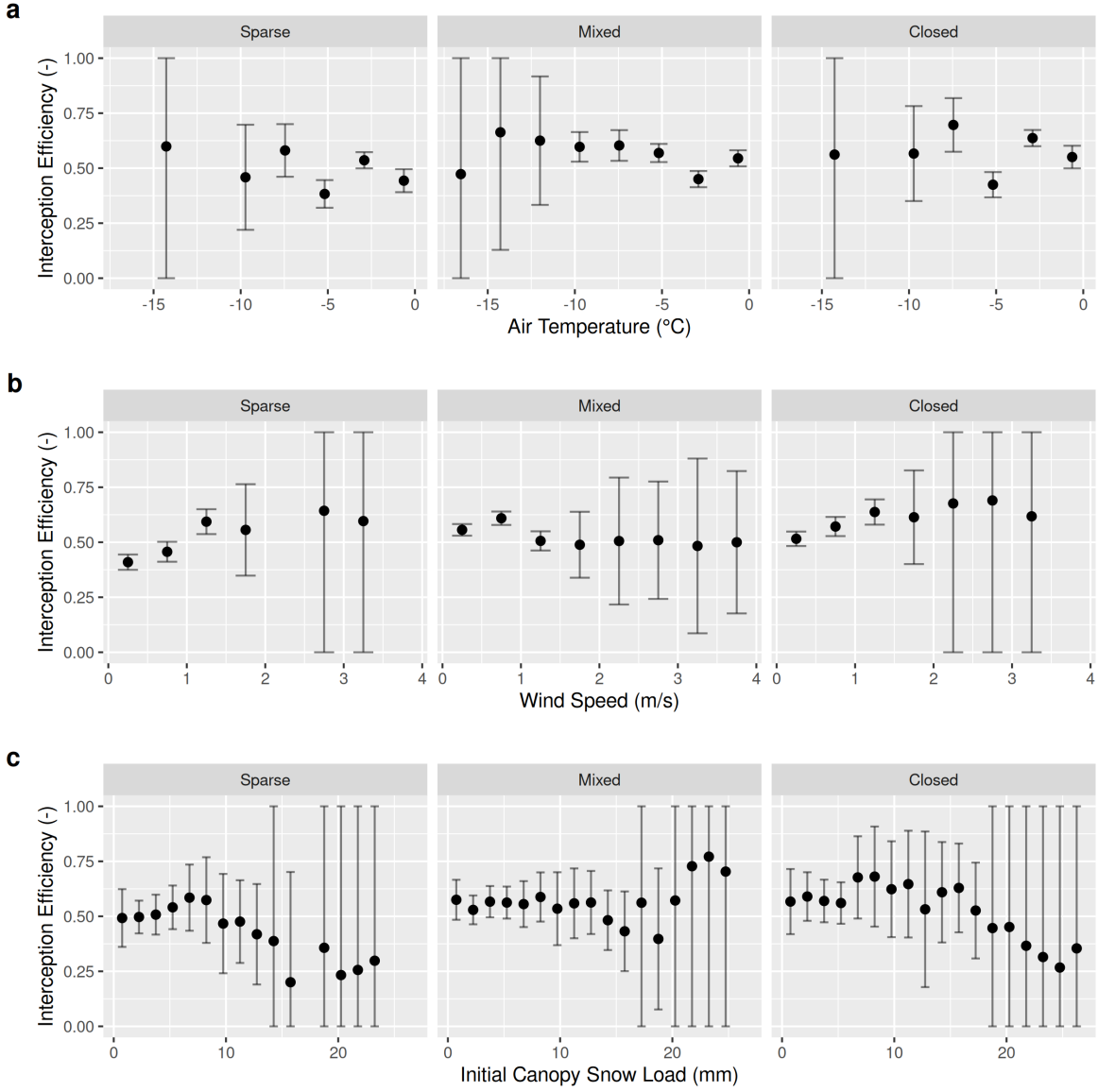


Figure 5: Scatter plots showing the interception efficiency calculated from accumulated snowfall (Pluvio) and throughfall (SCL) measurements for bins of air temperature, wind speed, and initial canopy snow load (the snow load observed by the weighed tree at the beginning of the timestep) over the 26 snowfall events. The error bars represent the estimated combined instrument error of the snowfall gauge and SCLs.

324 **4.2 The influence of canopy density on snow interception**

325 UAV-lidar measurements of throughfall and canopy density provide insights on how the forest
326 canopy influenced subcanopy snow accumulation during a wind-driven snowfall event between
327 March 13–14th. This event totaled 28.7 mm of snowfall at PWL station and was characterized
328 by a transition from low rates of snowfall and air temperatures near 0°C to higher rates of
329 snowfall by late afternoon on March 13th coinciding with air temperatures around -2.5 °C. An
330 average wind speed of 1.3 m s⁻¹ and direction of 188° was observed 4.3 m above the ground at
331 FT Station. The mean observed hydrometeor terminal velocity observed over the event was
332 0.9 m s⁻¹.

333 Throughfall depth measured by UAV-lidar was close to the 28 in-situ manual measurements
334 with a mean bias of -0.001 m and RMSE of 0.024 m. More details on the accuracy of UAV-lidar
335 snow depth measurements are provided in the supporting information section. Figure 6 shows
336 the spatial distribution of throughfall and interception efficiency at the PWL and FT forest
337 plots. Reduced throughfall and greater interception efficiency was observed on the north (lee)
338 side of individual trees, which may be due to non-vertical hydrometeor trajectories caused by
339 the steady southerly winds observed over this event. Transparent areas within the forest plots
340 in Figure 6 represent grid cells that did not have any lidar ground returns (e.g., under dense
341 canopy proximal to tree trunks) or were masked due to disturbance (e.g., walking paths in
342 clearings). Visual observations on March 13th and 14th confirmed non-vertical hydrometeor
343 trajectories and increased canopy snow loads were observed on the windward side of individual
344 trees. This effect is shown in Figure 6 to be more apparent in the PWL forest plot than the
345 FT forest plot. This may be attributed to the taller trees and higher canopy cover of the PWL
346 forest plot compared to the FT forest plot, as for the same trajectory angle a taller tree will
347 produce a larger downwind footprint.

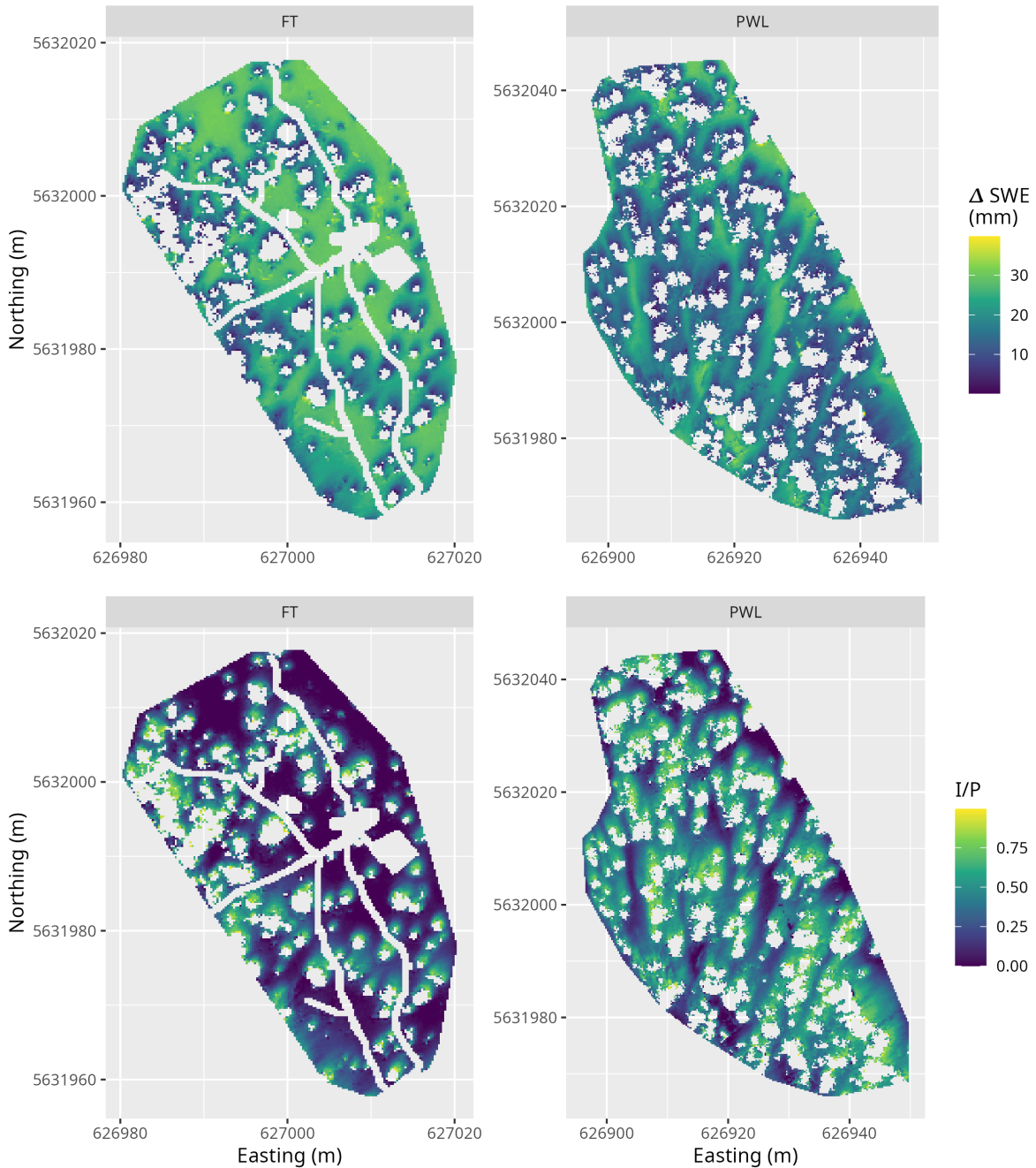


Figure 6: UAV-lidar measurements of the change in snow water equivalent, SWE (mm) and interception efficiency, I/P (-), over the March 13, 2023 24-hour snowfall event for the FT and PWL forest plots at a 0.25 m resolution. See the location of the two forest plots in Figure 1.

348 The VoxRS measurements of C_p on March 13th were selected for analysis and represents the
 349 canopy of both forest plots without snow. Little difference in C_p was observed between the
 350 March 13th and March 14th VoxRS measurements. Figure 7 shows a strong linear correlation
 351 between C_p measured on March 13th and interception efficiency towards the southern portion
 352 of the hemisphere, aligning with the average event wind direction. For the PWL forest plot,
 353 the upper 97.5th percentile of the ρ_p values shown in Figure 7, were found between azimuth
 354 angles of 167°–217°. Similarly, for the FT forest plot, the upper 97.5th percentile of the Pearson
 355 Correlation Coefficient (ρ_p) was found between azimuth angles of 171°–223°. The zenith angle
 356 found to have the highest correlation over this azimuth range was 22° ($\rho_p = 0.7$) and 21° (ρ_p
 357 = 0.83) for PWL and FT respectively. The high correlation coefficients found for non-vertical
 358 zenith angles for both PWL and FT are hypothesized to result from non-vertical hydrometeor
 359 trajectories.

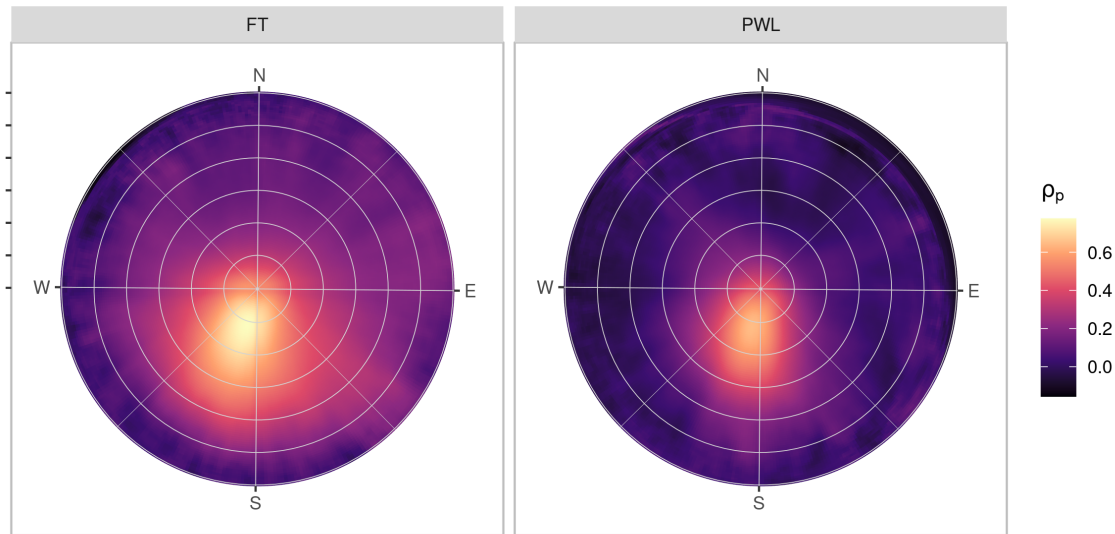


Figure 7: The Pearson Correlation Coefficient between rasters (0.25 m resolution) of interception efficiency and leaf contact area (measured on March 13th) for each grid cell across the study site for each azimuth angles (0°, 1°, ..., 359°) and zenith angles (0°, 1°, ..., 90°) for the FT (left) and PWL (right) forest plots.

360 An estimate of C_p for the event was selected from the VoxRS measurements based on the vector

361 corresponding to the azimuth and zenith angles observed to have the highest ρ_p in Figure 7.
 362 The spatial distribution of the selected VoxRS C_p measurements is shown in Figure 8 and
 363 generally aligns with the spatial distribution of interception efficiency and throughfall shown
 364 in Figure 6.

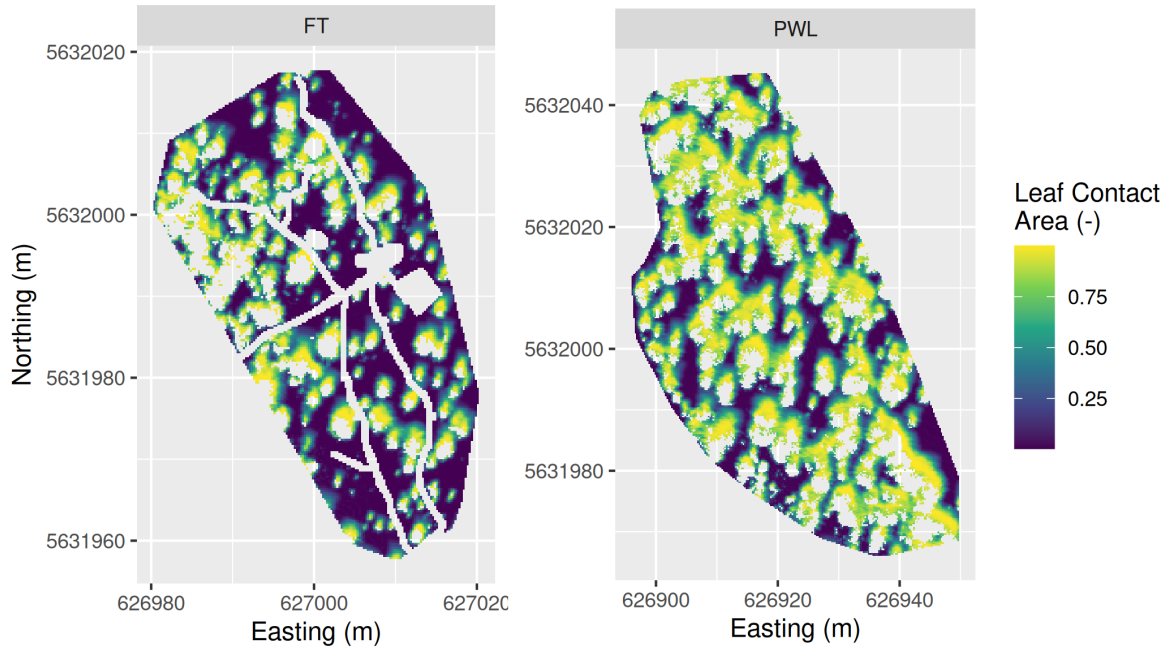


Figure 8: UAV-lidar VoxRS measurements of leaf contact area measured on March 13th for the PWL and FT forest plots for zenith angles (PWL = 22°, FT = 21°) and azimuth angles (PWL = 167°, 178°, ... 217°; FT = 171°, 172°, ... 223°).

365 Figure 9 shows the correlation between interception efficiency (Figure 6) and C_p (Figure 8),
 366 resampled to a 5 m grid resolution, was higher compared to the association with leaf contact
 367 angle measured at a zenith angle of 0°. The stronger association for the vector-based calculation
 368 suggests that adjusted C_p is a useful predictor of interception efficiency before ablation. An
 369 ordinary least squares linear regression forced through the origin was fit to the observed data

370 points using the following equation:

$$\frac{I}{P} = C_p(C_c, \theta_h) \cdot \alpha \quad (9)$$

371 where α is an efficiency constant which determines the fraction of snowflakes that contact the
 372 C_p elements and are stored in the canopy (e.g., intercepted) before canopy snow unloading or
 373 ablation processes begin.

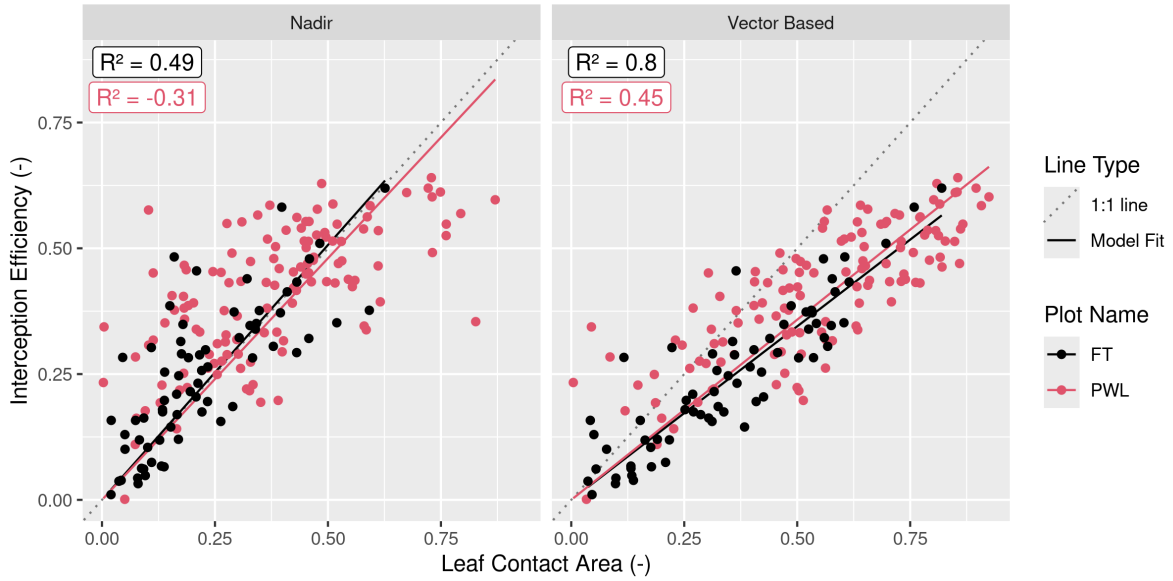


Figure 9: Scatter plots showing the relationship between leaf contact area and interception efficiency rasters resampled to a 5 m grid cell resolution. The left plot (nadir) shows leaf contact area measured from a zenith angle of 0°. The right plot (Vector Based) shows the leaf contact area averaged over rasters with zenith angles (PWL = 22°, FT = 21°) and azimuth angles (PWL = 167°, 178°, ... 217°; FT = 171°, 172°, ... 223°). The solid lines (Model fit) show an ordinary least squares linear regression forced through the origin and fitted to the PWL (red) and FT (black) data and the light grey dotted line shows a 1:1 line. The R^2 values for the four different models are shown in the upper left of each panel calculated following the methods outlined in Kozak & Kozak (1995).

374 For the vector-based model, the relationship between interception efficiency and C_p results in
 375 R^2 values of 0.45 and 0.8 for PWL and FT respectively. The increase in interception efficiency

376 with C_p follows a reduced slope compared to the nadir models with α values of 0.72 and 0.69
377 for the PWL and FT vector-based models respectively. The reduced slope for the vector-based
378 models may be due to snowflakes that weaved through and/or bounced off branch elements
379 in addition to UAV-lidar measurement uncertainty which may have been slightly affected by
380 unloading and redistribution. These processes would have reduced the fraction of snowfall
381 that was stored in the canopy. Model error statistics are presented in Table 3 for the nadir
382 and vector-based models and show the vector-based model provided a better prediction of
383 interception efficiency. Some of the scatter observed in the nadir model shown in Figure 9
384 may be explained by grid cells which observed a greater interception efficiency compared to
385 the corresponding C_c value and can be attributed to the inability of C_c to represent the
386 increase in interception observed within canopy gaps in Figure 6. Conversely, grid cells where
387 interception efficiency is less than C_c , may be affected by non-vertical trajectory hydrometeors
388 making their way underneath the canopy as observed by the reduced interception efficiency
389 on the windward edges of individual trees in Figure 6. The latter explanation suggests the
390 non-linear relationship observed for the PWL nadir calculation in Figure 6.

Table 3: Model error statistics provided for predictions of interception efficiency using Equation 9 and for different a values, as shown in the Model Slope column. Statistics are provided for the PWL and FT forest plots, using leaf contact area canopy metrics adjusted to zenith angles of ($0^\circ, 1^\circ, \dots 30^\circ$) and azimuth angles ($170^\circ, 171^\circ, \dots 220^\circ$) and nadir zenith angle of 0° . The Mean bias is the difference in the model and observed values, MAE is the mean of the absolute error, RMS Error is the root mean squared error, R^2 is the coefficient of determination adjusted using Equation 10 in Kozak & Kozak (1995).

Plot	Canopy	Model Slope	Mean Bias	MAE	RMS Error	
Name	Calculation	(-)	(-)	(-)	(-)	R^2
FT	Nadir	1.01	0.024	0.072	0.101	0.49
FT	Vector Based	0.69	0.003	0.047	0.063	0.80
PWL	Nadir	0.96	0.049	0.115	0.148	NA
PWL	Vector Based	0.72	0.020	0.079	0.096	0.45

391 **4.3 The combined influence of trajectory angle and canopy density on
392 interception**

393 Figure 10 shows that C_p , measured from VoxRS prior to snowfall on March 13th, increases
394 substantially with simulated hydrometeor trajectory angle and corresponding simulated wind
395 speed. The standard deviation in VoxRS measured C_p , illustrated by the shaded area in
396 Figure 10, exhibits the broad range in values for individual grid cells across each forest plot.
397 Despite this large scatter, a systematic increase in the mean C_p across both forest plots results
398 from a rise in the number of canopy elements for more horizontal angles, when averaged across
399 each forest plot, over all azimuth angles (see top left panel Figure 10). This results in a large
400 rise in C_p over relatively common estimated wind speeds. For example, with a wind speed
401 of 1 m s^{-1} and estimated trajectory angle of 48° , C_p would increase by 0.31 and 0.28 for the
402 PWL and FT forest plots respectively (Figure 10). This is a fractional increase in the plot C_p
403 from nadir of 0.61 and 0.95 for PWL and FT respectively. The increase in C_p from C_c , with
404 increasing trajectory angle is shown on the bottom row of Figure 10 and exhibits a similar

405 relationship for both forest plots FT and PWL until trajectory angles reach approximately
406 60° . Beyond 60° , the PWL rate of increase slows as the C_p approaches 1.0, while the FT plot,
407 which has lower C_c , continues to rise until around 75° as a C_p of 1.0 is approached. C_p was
408 also quantified across trajectory angles for both PWL and FT on March 14th, post snowfall,
409 and showed a negligible increase in C_p compared to C_p measured on March 13th without snow
410 in the canopy.

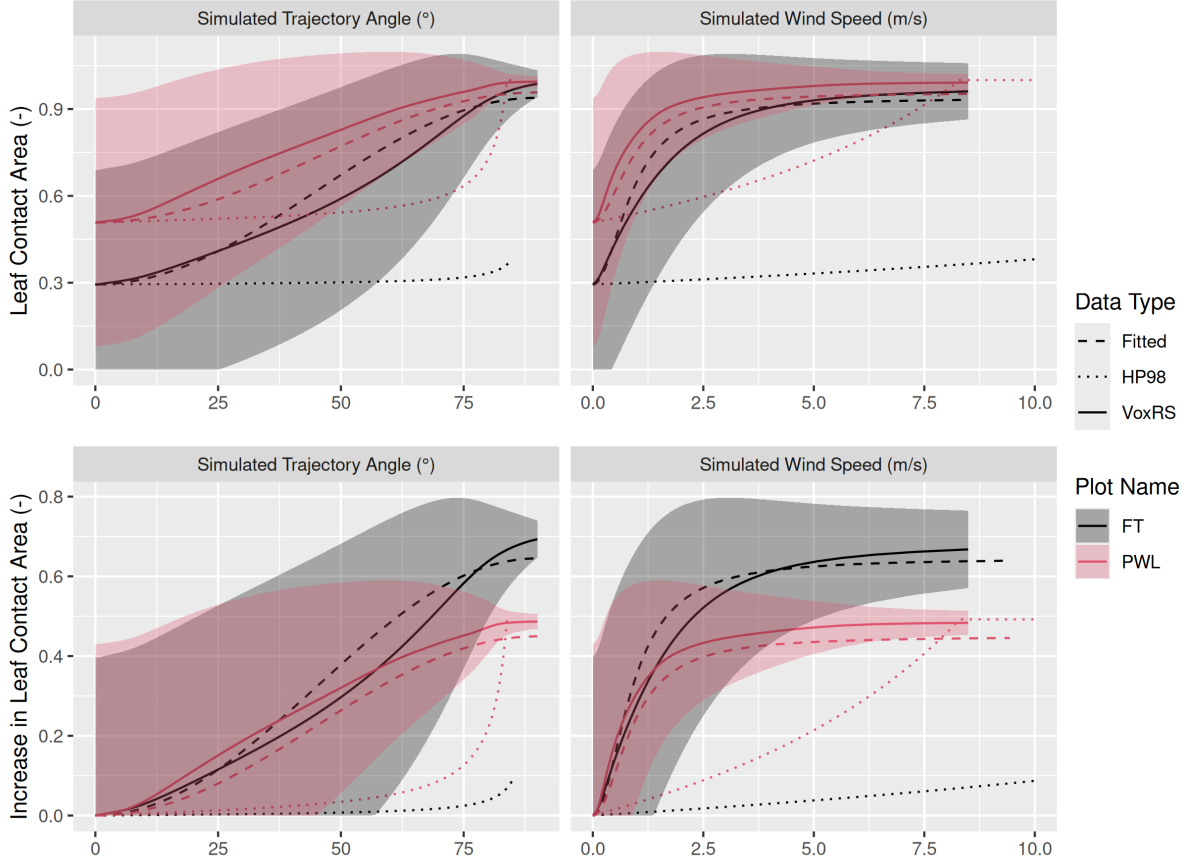


Figure 10: Plots showing the relationship between hydrometeor trajectory angle (left column) and wind speed (right column) with mean plot-wide snow-leaf contact area, C_p (top row) and the increase in mean plot-wide C_p , e.g., $C_p - C_c$ (bottom row). The simulated hydrometeor trajectory angle is measured as degrees from zenith. Simulated wind speed was calculated as a function of hydrometeor trajectory angle by rearranging Equation 4 and an observed event hydrometeor fall velocity of 0.9 m s^{-1} . The solid lines (VoxRS) represent the mean C_p (top row) or increase in mean C_p (bottom row) for a single zenith angle observed from VoxRS across all grid cells for each forest plot and across all azimuth angles. The shaded area represents 1 standard deviation above and below the observed VoxRS mean. The dashed lines (Fitted) represent predictions from Equation 10 (top row) and Equation 11 (bottom row). The dotted lines (HP98) represent the predictions from Equation 10 in Hedstrom & Pomeroy (1998). A forested downwind distance of 100 m was assumed for the HP98 calculation.

411 A function is proposed here to calculate plot-scale leaf contact area, C_p (-):

$$C_p = C_c + C_{inc}(\theta_h, C_c) \quad (10)$$

412 where, C_{inc} represents the increase in leaf contact area from C_c , and it is a function of θ_h .
 413 To estimate C_{inc} in the absence of detailed canopy measurements, the following function is
 414 proposed:

$$C_{inc} = (1 - C_c) \cdot f(\theta_h) \quad (11)$$

415 where $1 - C_c$ represents the void space in the canopy, and $f(\theta_h)$ is a function describes the
 416 relative increase in canopy area as a function of θ_h . Here, $f(\theta_h)$ is approximated as:

$$f(\theta_h) = b \cdot \sin(\theta_h)^2 \quad (12)$$

417 where b is a fitting coefficient, estimated to be ~ 0.91 through a non-linear least squares re-
 418 gression fit to the VoxRS measurements at both FT and PWL. The term $\sin(\theta_h)^2$ reflects the
 419 relative increase in snow-leaf contact area, which in turn leads to a proportional decrease in the
 420 canopy void space ($1 - C_c$). Thus, for θ_h of 0° , $f(\theta_h) = C_{inc} = 0$ and C_p is equal to the canopy
 421 coverage. In contrast, for θ_h close to 90° , C_p approaches a value of 1.0. The assumptions of
 422 Equation 12 include its application to a forest with relatively uniform structure (e.g., without
 423 large clear cuts) and where the mean height of the canopy is greater than the mean width
 424 of individual trees. Additionally, it is assumed that snowfall is not transmitted through the
 425 canopy and that overlapping of canopy elements is negligible.

426 Simulated C_p using Equation 10 is shown in the dashed lines in the top row of Figure 10
 427 and follows the VoxRS-measured mean C_p closely. Model error statistics shown in Table 4
 428 demonstrate that Equation 11 performed well, with a mean bias and RMSE of (-) and (-)
 429 respectively for PWL, and (-) and (-) for FT. In contrast, Table 4 reveals that the Hedstrom
 430 & Pomeroy (1998) method produced significantly less accurate estimates of C_p , with a mean

⁴³¹ bias and RMSE of -0.2 (-) and 0.23 (-) respectively for PWL, and -0.26 (-) and 0.32 (-) for
⁴³² FT.

Table 4: Model error statistics calculated for the prediction of leaf contact area from trajectory angle using Equation 11 (Eq. 11) and Equation 10 from Hedstrom & Pomeroy (1998) for the PWL and FT forest plots. Mean bias is the difference in the model and observed values, MAE is the mean of the absolute error, RMS Error is the root mean squared error and R^2 is the coefficient of determination. The units for all metrics are dimensionless. A forested downwind distance of 100 m was used for the HP98 calculation.

Model	Plot Name	Mean Bias (-)	MAE (-)	RMS Error (-)	R^2
HP98	FT	-0.26	0.26	0.32	-0.97
HP98	PWL	-0.20	0.20	0.23	-0.96
Eq. 10	FT	0.03	0.04	0.05	0.95
Eq. 10	PWL	-0.05	0.05	0.05	0.90

⁴³³ 4.4 Throughfall model performance

⁴³⁴ The performance of the interception efficiency (Equation 9) and leaf contact area (Equation 10)
⁴³⁵ parameterizations in estimating event throughfall was assessed against UAV-lidar measure-
⁴³⁶ ments of throughfall at the plot scale for the March 13–14th snowfall event. In this assessment,
⁴³⁷ the hydrometeor trajectory angle was approximated using Equation 4 combined with the mean
⁴³⁸ event wind speed at one-third the mean canopy height (estimated from Equation 5 and the
⁴³⁹ observed wind speed at FT station) and hydrometeor terminal velocity (measured at PWL
⁴⁴⁰ station). Leaf contact area was then estimated using Equation 10 for the PWL and FT plots,
⁴⁴¹ incorporating the approximated hydrometeor trajectory angle and observed canopy coverage
⁴⁴² from the VoxRS dataset. Interception efficiency was calculated using Equation 9 with the
⁴⁴³ estimated leaf contact area and accumulated snowfall measured at PWL station for the event.
⁴⁴⁴ An α value, used in Equation 9, of 0.978 (-) was found through calibration which provided the
⁴⁴⁵ best fit between observed and simulated interception efficiency at the plot scale for both FT

⁴⁴⁶ and PWL.

⁴⁴⁷ Figure 11 illustrates that the new vector-based parameterization closely matches UAV-lidar
⁴⁴⁸ measurements of throughfall. Modelled throughfall from the vector-based model was 17.2 mm
⁴⁴⁹ compared to the measured throughfall of 16.6 mm for PWL. For FT, the vector-based mod-
⁴⁵⁰ elled throughfall was 21.5 mm, while the measured values were 22.1 mm. Table 5 presents
⁴⁵¹ both observed and modelled values for interception efficiency and throughfall, along with cor-
⁴⁵² responding error statistics. The vector-based model shows a lower mean bias of -0.6 mm for
⁴⁵³ PWL and 0.6 mm for FT, in contrast to the nadir-based model, which overestimated through-
⁴⁵⁴ fall for both plots. This overestimation occurred because the nadir-based model approximated
⁴⁵⁵ leaf contact area directly from canopy cover measurements (i.e., was not adjusted using Equa-
⁴⁵⁶ tion 10), resulting in a lower estimated contact area and consequently less snow intercepted
⁴⁵⁷ in the canopy.

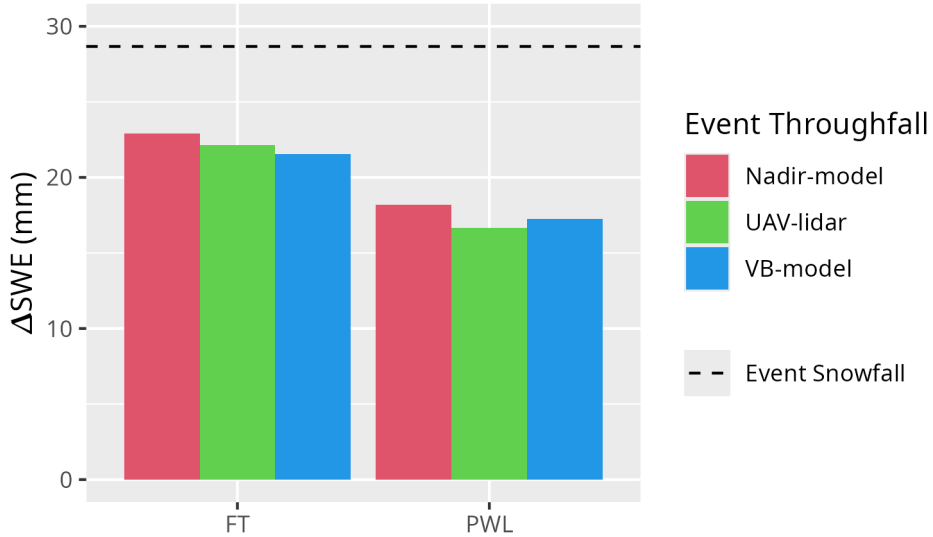


Figure 11: Bar chart comparing the observed and modelled mean change in throughfall (ΔSWE , mm) over the March 13-14th snowfall event averaged over forest plots FT and PWL. The ‘Nadir-model’ used Equation 9 not adjusted for trajectory angle (e.g., C_c) and the Vector-based ‘VB-model’ which uses Equation 9 with C_p adjusted for trajectory angle. ‘UAV-lidar’ corresponds to throughfall calculated using Equation 6 incorporating UAV-lidar snow depth and snow density from in-situ snow pits. The black horizontal dashed line shows the accumulated SWE (mm) over the snowfall event to the PWL station open clearing.

Table 5: Model error statistics for model estimates of snow interception efficiency (I/P) and throughfall (TF) compared to measurements of I/P and TF using UAV-lidar averaged over the FT and PWL forest plots. Units for I/P are (-) and TF are (mm). The vector-based model utilized Equation 9 with C_p adjusted for trajectory angle. The nadir model also utilized Equation 9 but was not adjusted for trajectory angle and thus C_c was used instead of C_p . The ‘Obs. Value’ column contains measurements from UAV-lidar while the ‘Mod. Value’ column contains the modelled values. The mean bias was calculated as observed minus modelled and percent error is the percent error between predicted and observed values.

	Model	Value		Obs.	Mod.	Mean	
Plot	Type	Name	Units	Value	Value	Bias	Perc. Error
FT	VB-model	I/P	-	0.23	0.25	-0.02	-9.01
FT	Nadir-model	I/P	-	0.23	0.20	0.03	12.10
FT	VB-model	TF	mm	22.12	21.53	0.59	2.67
FT	Nadir-model	TF	mm	22.12	22.91	-0.79	-3.58
PWL	VB-model	I/P	-	0.42	0.40	0.02	4.91
PWL	Nadir-model	I/P	-	0.42	0.37	0.05	12.95
PWL	VB-model	TF	mm	16.64	17.24	-0.59	-3.55
PWL	Nadir-model	TF	mm	16.64	18.20	-1.56	-9.35

458 **5 Discussion**

459 **5.1 Influence of Air Temperature, Wind Speed and Canopy Snow Load on Initial
460 Interception**

461 The point scale observations presented in Figure 5 indicate that air temperature had little
462 influence on initial interception efficiency during periods were melt and unloading of snow
463 were less likely. This finding aligns with Storck et al. (2002), who observed that variations
464 in air temperature did not significantly affect interception efficiency for measurements that
465 partitioned ablation and initial canopy snow loading processes. The limited association may
466 be explained as air temperature influences processes that both increase or decrease interception
467 efficiency, which may occur simultaneously and limit the overall effect. For example, warmer
468 temperatures increase branch flexibility (Schmidt & Gluns, 1991), and can cause snow loaded
469 branches to bend and thus reduce C_p . In contrast, the cohesion and adhesion of snowfall
470 has been shown to increase for warmer temperatures (Kobayashi, 1987; Pfister & Schneebeli,
471 1999) which could increase the efficiency constant (i.e., α in Equation 9) thereby increasing
472 interception efficiency as observed by Katsushima et al. (2023). However, the throughfall
473 observations reported here were filtered to exclude periods of canopy snow melt, when higher
474 liquid water content enhances cohesion and adhesion, and liquid water may freeze onto the
475 canopy. Therefore, the α value reported here may be less compared to other environments that
476 experience significant snowfall near the melting point. However, the combination of Equation 9
477 with an energy balance based canopy snow melt routine could also help represent the refreezing
478 of snow to the canopy.

479 A weak trend was observed between initial interception efficiency (i.e., before unloading) with
480 increasing wind speed at two locations which were sheltered from the predominant wind di-
481 rection (Figure 6b). This is attributed to an associated increase in C_p due to non-vertical
482 hydrometeor trajectories. These results are consistent with observations by Schmidt & Troen-
483 dle (1989) who observed a slight increase in snowfall interception with increasing wind speeds

⁴⁸⁴ up to 6 m s⁻¹ and studies of rainfall interception by Herwitz & Slye (1995) and Van Stan et al.
⁴⁸⁵ (2011).

⁴⁸⁶ The slight increase in interception efficiency for smaller canopy snow loads and decline for
⁴⁸⁷ larger canopy snow loads is attributed to the influence of canopy snow load on C_p (Figure 6c).
⁴⁸⁸ While small, this effect is consistent with the theory proposed by Satterlund & Haupt (1967)
⁴⁸⁹ that interception efficiency increases as the canopy fills with snow bridging gaps in the canopy,
⁴⁹⁰ while later declining due to branch bending and decreased canopy cover. However, at the
⁴⁹¹ plot-scale Staines & Pomeroy (2023), show that these two processes may partially compensate
⁴⁹² for each other as C_p increases for closed canopies, as new snow bridges gaps, but decreases in
⁴⁹³ partially open canopy due to branch bending (i.e., Fig. 2 in Schmidt & Gluns, 1991). The
⁴⁹⁴ increase in C_p resulting from snow load in Staines & Pomeroy (2023) was small compared to
⁴⁹⁵ the substantial rise in C_p due to trajectory angle presented in their study. Which corroborates
⁴⁹⁶ with the plot-scale observations of C_p in this study shown in Figure 10. Moreover, additional
⁴⁹⁷ studies (Calder, 1990; Watanabe & Ozeki, 1964) align with the observations in Figure 3, which
⁴⁹⁸ show a relatively linear increase in canopy snow load with increasing snowfall. Further evidence
⁴⁹⁹ in support of the relatively small influence of canopy snow load on C_p , is provided by Lundquist
⁵⁰⁰ et al. (2021) who reported improved simulation of subcanopy snow accumulation without the
⁵⁰¹ use of a maximum canopy snow load, when linked with a comprehensive canopy snow ablation
⁵⁰² routine. Lehtonen et al. (2016) also note that in northern Finland heavy canopy snow loads
⁵⁰³ have been observed to continue increasing until stem breakage, under conditions favourable
⁵⁰⁴ for the formation of significant rime-ice accretion and limited ablation, thus reducing C_p .
⁵⁰⁵ Models are available to predict the accretion of ice on tree canopies (e.g., Nock et al., 2016)
⁵⁰⁶ however, further research is required to understand the canopy snow load required to cause
⁵⁰⁷ stem breakage across different tree species and canopy loads. The low sensitivity of interception
⁵⁰⁸ efficiency with canopy snow load found in this study and others may be attributed to several
⁵⁰⁹ factors: a reduced inclusion of ablation processes in the interception efficiency measurements,
⁵¹⁰ limited influence of canopy snow load on C_p at this study site, and/or the compensatory effects
⁵¹¹ outlined by Satterlund & Haupt (1967).

512 **5.2 Justification for and Limitations of a New Snow Interception Model**

513 The limited influence of air temperature and canopy snow load on initial interception reported
514 here differs from the theories underpinning existing snow interception parameterizations (Hed-
515 strom & Pomeroy, 1998; Moeser et al., 2015; Satterlund & Haupt, 1967; Storck et al., 2002).
516 Cebulski & Pomeroy (2025) highlights the uncertainty in the extent to which ablative processes
517 are included in common snow interception models. Since canopy snow ablation is strongly re-
518 lated to air temperature and snow load (Ellis et al., 2010; Floyd, 2012; Hedstrom & Pomeroy,
519 1998; Roesch et al., 2001) some the previously observed relationships related to these variables
520 may be explained by changes in ablation rather than initial interception. Moreover, since a
521 canopy snow load capacity was not observed in this study, the air temperature dependent
522 canopy snow load capacities included in the Hedstrom & Pomeroy (1998) and Andreadis et
523 al. (2009) models were not applicable. Studies that have identified a relationship between air
524 temperature and interception efficiency (Katsushima et al., 2023; Roth & Nolin, 2019), were
525 not explicitly focused on initial interception, prior to canopy snow ablation, and therefore
526 include ablation processes in their measurements. Consequently, the relationships reported in
527 Roth & Nolin (2019) and Katsushima et al. (2023) result from initial interception and abla-
528 tion processes. Similarly, the decrease in interception efficiency with increasing canopy snow
529 load reported in Schmidt & Gluns (1991) and Katsushima et al. (2023) may be complicated
530 by canopy snow ablation processes. The coupling of ablation processes within existing snow
531 interception models may contribute to overestimates of throughfall, canopy snow unloading,
532 and canopy snow melt when combined with other canopy snow ablation parameterizations
533 (Cebulski & Pomeroy, 2025).

534 To address these issues, a new vector-based snow interception parameterization, Equation 9,
535 is presented which calculates initial interception efficiency as a function of C_p and α . This
536 new parameterization allows for canopy snow loading processes to be isolated from canopy
537 snow ablation processes and is consistent with current rainfall interception theory (Valante
538 et al., 1997). Equation 9 differs only slightly from the original Hedstrom & Pomeroy (1998)

parameterization (see Equation 6 in Hedstrom & Pomeroy 1998), in that it does not calculate interception efficiency as a function of canopy snow load and from the Storck et al. (2002) parameterization who found interception efficiency to be constant. The theoretical basis of the α parameter in Equation 9 is that the association between C_p and interception efficiency, as shown in Figure 9, unlike existing rainfall parameterizations (Valante et al., 1997) does not follow a 1:1 line, as falling snow hydrometeors may bounce off the canopy elements. Further research is needed to explore how processes such as the increased cohesion and adhesion of snowfall to the canopy at warm temperatures, as observed by Kobayashi (1987), Pfister & Schneebeli (1999), as well as hydrometeor velocity, particle size, and shape suggested by (Katsumi et al., 2023), may influence the α parameter, although these effects were not observed in this study. Moreover, the relationship of C_p with air temperature and canopy snow load is expected to vary across varying combinations of climate, forest structure, species, and ages, requiring further research. For example, certain tree species or ages with very flexible branches may warrant the explicit representation of variable C_p with canopy snow load. Since Equation 9 intentionally excludes processes attributed to canopy snow ablation that were previously included in earlier snow interception models, these ablation processes must be incorporated in canopy snow ablation parameterizations to fully represent the canopy snow mass balance.

Measurements of interception efficiency, as shown in Figure 6, align with the theory proposed by Hedstrom & Pomeroy (1998) which suggests reduced throughfall on the lee side of individual trees for a wind driven snowfall event. However, an existing exponential relationship proposed in Hedstrom & Pomeroy (1998) to scale C_p with wind speed failed to reproduce the observations presented in Figure 10. Instead, plot-wide C_{inc} was found to increase as function of θ_h and C_c . Significant scatter in VoxRS measured C_p across the two forest plots, illustrated by the high standard deviation in Figure 10, resulted from variability in canopy density across different locations and azimuth angles. This large scatter suggests the observed relationships in Figure 10 are only applicable at the forest stand scale where the sub-metre variability in C_p averages out. Figure 10 shows that at the plot scale, C_p rises with increasing θ_h , as there is a greater number of grid cells which have more closed canopy at more horizontal angles. Still,

567 Equation 11 would not be applicable in areas that have large continuous gap fractions (e.g.,
568 large forested clear cuts) that are many times wider than the mean canopy height. Further
569 testing of Equation 11 is also needed in a wide range of forest species, ages, densities, and
570 structures. Staines & Pomeroy (2023) have also shown that backflows and large eddies that
571 occur within the canopy can also contribute to mixed responses.

572 It was found that the mean event hydrometeor trajectory angle, required for Equation 11, could
573 be predicted from Equation 4 using the observed mean hydrometeor fall velocity and the mean
574 horizontal wind speed selected at one-third of the canopy height above the ground. A wind
575 speed at one-third the mean canopy height is hypothesized to be important for canopy snow
576 accumulation as a large fraction of the horizontal cross-sectional area is at this height for most
577 needleleaf canopies. Katsushima et al. (2023), also proposed the wind speed at one-third the
578 canopy height for modelling unloading of canopy snow as it corresponds to the centre of gravity
579 when the horizontal projection of the canopy is assumed to be a triangle. However, there is
580 uncertainty in the transferability of the canopy height observed here to other environments
581 due to differing forest structures and tree species. This may include forests with a larger trunk
582 space or have more of their canopy contact area at higher heights above the ground (e.g., some
583 deciduous canopies). Moreover, Equation 4 assumes a linear hydrometeor trajectory, and does
584 not consider non-linear patterns such as wind flow directions around tree elements, turbulent
585 flow, or differences in wind speed with height.

586 Although the improvement in performance of the vector-based model over the nadir model was
587 relatively small, the vector-based model is preferred due to its overall lower error compared
588 to the UAV-lidar measurements and better representation of physical processes. While the
589 vector-based model acts to increase interception efficiency with wind speed, several studies
590 have shown that canopy snow ablation increases as a result of wind induced unloading (Bartlett
591 & Verseghy, 2015; Betts & Ball, 1997; Lumbrago et al., 2022; Roesch et al., 2001; Wheeler,
592 1987). Thus, representing both the increase in initial interception due to inclined hydrometeor
593 trajectory angles and the subsequent increase in canopy snow unloading will be important
594 in subcanopy snow accumulation models. This new vector-based model has been developed

and tested based at the forest plot scale (hectares) and is therefore currently suitable for application in hydrological models at this scale that are discretized by forest density. Previous models were developed based on process understanding at varying scales: Hedstrom & Pomeroy (1998), based on snow survey transects at the forest plot scale (intervals ranging from days to weeks), and Storck et al. (2002), based on point-scale 30-minute interval lysimetry observations. Recent evidence from Staines & Pomeroy (2023) and the results presented here suggest that some of the process understanding developed in previous studies may not be applicable at larger scales or finer spatial and temporal resolutions. Therefore, the process understanding presented here may be more suitable for application at larger extents and finer temporal resolutions, however, further testing is required to support this theory.

6 Conclusions

New observations of initial snow interception, collected over a wide range of meteorological conditions and canopy densities indicate that forest is the primary factor influencing subcanopy snow accumulation. At the point scale, measurements revealed no evidence of a maximum canopy snow load, even for event snowfalls up to 45 mm, nor was there any indication of air temperature influencing the cohesion and adhesion of snowfall to the canopy or branch bending reducing canopy cover. Instead, wind speed was found to influence interception efficiency by changing the hydrometeor trajectory angle, which can lead to a substantial increase in snow-leaf contact area.

At the forest plot scale, UAV-lidar measurements of throughfall aligned with the point-scale observations demonstrating that leaf contact area was the primary factor influencing interception efficiency at a particular site. Leaf contact area, which incorporates changes in the number of canopy contacts with hydrometeor trajectory angle, proved to be a better predictor of interception efficiency compared to nadir-calculated canopy cover. When averaged across each forest plot, leaf contact area was shown to be highly sensitive to trajectory angle, increasing by 61–95% for trajectory angles associated with a 1 m s^{-1} wind speed. An existing

621 theoretical relationship failed to adequately represent the VoxRS-measured increase in leaf
622 contact area with simulated trajectory angles. As a result, a new relationship is proposed as a
623 function of canopy cover and hydrometeor trajectory angle (approximated from wind speed),
624 which demonstrated good performance at this study site.

625 The weak association between air temperature and canopy snow load with interception effi-
626 ciency, as presented here and in other recent studies, coupled with the influence of wind speed
627 on leaf contact area, highlights the need for a new snow interception parameterization. A new
628 parameterization is proposed that calculates initial interception as a function of snowfall and
629 leaf contact area. This parameterization is consistent with rainfall interception studies, which
630 also separate canopy loading and ablation processes, and calculate interception as a function
631 of canopy cover. Additionally, a second equation is proposed to estimate leaf contact area
632 as a function of hydrometeor trajectory angle and nadir canopy cover. This updated snow
633 interception parameterization performed well in the subalpine forest studied here at the forest
634 plot scale. However, further validation is necessary in a range of climates, forests, and larger
635 spatial extents.

636 **7 Acknowledgments**

637 We wish to acknowledge financial support from the University of Saskatchewan Dean's Schol-
638 arship, Natural Sciences and Engineering Research Council of Canada, Global Water Futures
639 Programme, Environment and Climate Change Canada, Alberta Innovates, Canada Founda-
640 tion for Innovation, and the Canada Research Chairs Programme. We thank Madison Harasyn,
641 Hannah Koslowsky, Kieran Lehan, Lindsey Langs and Fortress Mountain Resort for their help
642 in the field. Jacob Staines, Madison Harasyn, Alistair Wallace, and Rob White contributed
643 to developing the UAV-lidar processing workflow.

⁶⁴⁴ **8 Data Availability**

⁶⁴⁵ The data that support the findings in this study are available at <https://doi.org/10.5281/zenodo.14018893>.

646 **References**

- 647 Andreadis, K. M., Storck, P., & Lettenmaier, D. P. (2009). Modeling snow accumulation
648 and ablation processes in forested environments. *Water Resources Research*, 45(5), 1–33.
649 <https://doi.org/10.1029/2008WR007042>
- 650 Bartlett, P. A., & Verseghy, D. L. (2015). Modified treatment of intercepted snow improves
651 the simulated forest albedo in the Canadian Land Surface Scheme. *Hydrological Processes*,
652 29(14), 3208–3226. <https://doi.org/10.1002/HYP.10431>
- 653 Betts, A. K., & Ball, J. H. (1997). Albedo over the boreal forest. *Journal of Geophysical
654 Research: Atmospheres*, 102(D24), 28901–28909. <https://doi.org/10.1029/96JD03876>
- 655 Calder, I. R. (1990). *Evaporation in the uplands* (p. 148). Wiley.
- 656 Cebulski, A. C., & Pomeroy, J. W. (2025). Theoretical Underpinnings of Snow Interception
657 and Canopy Snow Ablation Parameterisations. *WIREs Water*, 12(e70010). [https://doi.or
g/10.1002/wat2.70010](https://doi.or
658 g/10.1002/wat2.70010)
- 659 Chianucci, F., & Macek, M. (2023). hemispheR: An R package for fisheye canopy image
660 analysis. *Agricultural and Forest Meteorology*.
- 661 Cionco, R. M. (1965). A mathematical model for air flow in a vegetative canopy. *Journal of
662 Applied Meteorology* (1962), 4(4), 517–522. [https://doi.org/10.1175/1520-0450\(1965\)004
%3C0517:AMMFAF%3E2.0.CO;2](https://doi.org/10.1175/1520-0450(1965)004
663 %3C0517:AMMFAF%3E2.0.CO;2)
- 664 Ellis, C. R., Pomeroy, J. W., Brown, T., & MacDonald, J. (2010). Simulation of snow accumu
665 lation and melt in needleleaf forest environments. *Hydrology and Earth System Sciences*,
666 14(6), 925–940. <https://doi.org/10.5194/hess-14-925-2010>
- 667 Ellis, C. R., Pomeroy, J. W., & Link, T. E. (2013). Modeling increases in snowmelt yield and
668 desynchronization resulting from forest gap-thinning treatments in a northern mountain
669 headwater basin. *Water Resources Research*, 49(2), 936–949. [https://doi.org/10.1002/wr
cr.20089](https://doi.org/10.1002/wr
670 cr.20089)
- 671 Essery, R., Pomeroy, J. W., Parviainen, J., & Storck, P. (2003). Sublimation of snow from
672 coniferous forests in a climate model. *Journal of Climate*, 16(11), 1855–1864. [https://doi.org/10.1175/1520-0442\(2003\)016%3C1855:SOSFCF%3E2.0.CO;2](https:
673 //doi.org/10.1175/1520-0442(2003)016%3C1855:SOSFCF%3E2.0.CO;2)

- 674 Floyd, W. C. (2012). *Snowmelt energy flux recovery during rain-on-snow in regenerating forests*
675 (p. 180) [PhD thesis, University of British Columbia]. <https://doi.org/https://dx.doi.org/10.14288/1.0073024>
- 676
- 677 Fryer, B. Y. G. I., Johnson, E. A., Fryer, G. I., & Johnson, E. A. (1988). Reconstructing
678 fire behaviour and effects in a subalpine forest. *The Journal of Applied Ecology*, 25(3),
679 1063–1072. <https://doi.org/10.2307/2403766>
- 680 Gelfan, A. N., Pomeroy, J. W., & Kuchment, L. S. (2004). Modeling forest cover influences on
681 snow accumulation, sublimation, and melt. *Journal of Hydrometeorology*, 5(5), 785–803.
682 [https://doi.org/10.1175/1525-7541\(2004\)005%3C0785:MFCIOS%3E2.0.CO;2](https://doi.org/10.1175/1525-7541(2004)005%3C0785:MFCIOS%3E2.0.CO;2)
- 683 Golding, D. L., & Swanson, R. H. (1978). Snow accumulation and melt in small forest openings
684 in Alberta. *Canadian Journal of Forest Research*, 8(4), 380–388. <https://doi.org/10.1139/x78-057>
- 685
- 686 Harder, P., & Pomeroy, J. W. (2013). Estimating precipitation phase using a psychrometric
687 energy balance method. *Hydrological Processes*, 27(13), 1901–1914. <https://doi.org/10.1002/hyp.9799>
- 688
- 689 Harder, P., Pomeroy, J. W., & Helgason, W. D. (2020). Improving sub-canopy snow depth
690 mapping with unmanned aerial vehicles: Lidar versus structure-from-motion techniques.
691 *The Cryosphere*, 14(6), 1919–1935. <https://doi.org/10.5194/tc-14-1919-2020>
- 692
- 693 Harpold, A. A., Krogh, S. A., Kohler, M., Eckberg, D., Greenberg, J., Sterle, G., & Broxton,
694 P. D. (2020). Increasing the efficacy of forest thinning for snow using high-resolution
695 modeling: A proof of concept in the Lake Tahoe Basin, California, USA. *Ecohydrology :
696 Ecosystems, Land and Water Process Interactions, Ecohydrogeomorphology*, 13(4). <https://doi.org/10.1002/eco.2203>
- 697
- 698 Hedstrom, N. R., & Pomeroy, J. W. (1998). Measurements and modelling of snow interception
699 in the boreal forest. *Hydrological Processes*, 12(10-11), 1611–1625. [https://doi.org/10.1002/\(SICI\)1099-1085\(199808/09\)12:10/11%3C1611::AID-HYP684%3E3.0.CO;2-4](https://doi.org/10.1002/(SICI)1099-1085(199808/09)12:10/11%3C1611::AID-HYP684%3E3.0.CO;2-4)
- 700
- 701 Herwitz, S. R., & Slye, R. E. (1995). Three-dimensional modeling of canopy tree interception
702 of wind-driven rainfall. *Journal of Hydrology*, 168(1-4), 205–226. [https://doi.org/10.1016/0022-1694\(94\)02643-P](https://doi.org/10.1016/0022-1694(94)02643-P)

- 703 Isyumov, N. (1971). *An approach to the prediction of snow loads* [PhD thesis]. The University
704 of Western Ontario (Canada).
- 705 Katsushima, T., Kato, A., Aiura, H., Nanko, K., Suzuki, S., Takeuchi, Y., & Murakami, S.
706 (2023). Modelling of snow interception on a Japanese cedar canopy based on weighing
707 tree experiment in a warm winter region. *Hydrological Processes*, 37(6), 1–16. <https://doi.org/10.1002/hyp.14922>
- 708 Kim, E., Gatebe, C., Hall, D., Newlin, J., Misakonis, A., Elder, K., Marshall, H. P., Hiem-
709 stra, C., Brucker, L., De Marco, E., Crawford, C., Kang, D. H., & Entin, J. (2017).
710 NASA's snowex campaign: Observing seasonal snow in a forested environment. *2017
711 IEEE International Geoscience and Remote Sensing Symposium (IGARSS)*, 1388–1390.
712 <https://doi.org/10.1109/IGARSS.2017.8127222>
- 713 Kobayashi, D. (1987). Snow accumulation on a narrow board. *Cold Regions Science and
714 Technology*, 13(3), 239–245. [https://doi.org/10.1016/0165-232X\(87\)90005-X](https://doi.org/10.1016/0165-232X(87)90005-X)
- 715 Kozak, A., & Kozak, R. A. (1995). Notes on regression through the origin. *Forestry Chronicle*,
716 71(3), 326–330. <https://doi.org/10.5558/tfc71326-3>
- 717 Langs, L. E., Petrone, R. M., & Pomeroy, J. W. (2020). A $\delta^{18}\text{O}$ and $\delta^2\text{H}$ stable water
718 isotope analysis of subalpine forest water sources under seasonal and hydrological stress
719 in the Canadian Rocky Mountains. *Hydrological Processes*, 34(26), 5642–5658. <https://doi.org/10.1002/hyp.13986>
- 720 Lehtonen, I., Kämärainen, M., Gregow, H., Venäläinen, A., & Peltola, H. (2016). Heavy snow
721 loads in Finnish forests respond regionally asymmetrically to projected climate change.
722 *Natural Hazards and Earth System Sciences*, 16(10), 2259–2271. <https://doi.org/10.5194/nhess-16-2259-2016>
- 723 Lumbrazo, C., Bennett, A., Currier, W. R., Nijssen, B., & Lundquist, J. (2022). Evalu-
724 ating multiple canopy-snow unloading parameterizations in SUMMA with time-lapse
725 photography characterized by citizen scientists. *Water Resources Research*, 58(6), 1–22.
726 <https://doi.org/10.1029/2021WR030852>
- 727 Lundberg, A., & Hallidin, S. (1994). Evaporation of intercepted snow: Analysis of governing
728 factors. *Water Resources Research*, 30(9), 2587–2598.
- 729

- 732 Lundquist, J. D., Dickerson-Lange, S., Gutmann, E., Jonas, T., Lumbrago, C., & Reynolds, D.
733 (2021). Snow interception modelling: Isolated observations have led to many land surface
734 models lacking appropriate temperature sensitivities. *Hydrological Processes*, 35(7), 1–20.
735 <https://doi.org/10.1002/hyp.14274>
- 736 MacDonald, J. P. J. (2010). *Unloading of intercepted snow in conifer forests* (Master of
737 {{Science}}) August; pp. 0–93). University of Saskatchewan.
- 738 Moeser, D., Stähli, M., & Jonas, T. (2015). Improved snow interception modeling using
739 canopy parameters derived from airborne LiDAR data. *Water Resources Research*, 51(7),
740 5041–5059. <https://doi.org/10.1002/2014WR016724>
- 741 Musselman, K. N., Pomeroy, J. W., & Link, T. E. (2015). Variability in shortwave irradiance
742 caused by forest gaps: Measurements, modelling, and implications for snow energetics.
743 *Agricultural and Forest Meteorology*, 207, 69–82. <https://doi.org/10.1016/j.agrformet.2015.03.014>
- 744 Nock, C. A., Lecigne, B., Taugourdeau, O., Greene, D. F., Dauzat, J., Delagrange, S., &
745 Messier, C. (2016). Linking ice accretion and crown structure: Towards a model of the
746 effect of freezing rain on tree canopies. *Annals of Botany*, 117(7), 1163–1173. <https://doi.org/10.1093/aob/mcw059>
- 747 Parviainen, J., & Pomeroy, J. W. (2000). Multiple-scale modelling of forest snow sublimation:
748 Initial findings. *Hydrological Processes*, 14(15), 2669–2681. [https://doi.org/10.1002/1099-1085\(20001030\)14:15%3C2669::AID-HYP85%3E3.0.CO;2-Q](https://doi.org/10.1002/1099-1085(20001030)14:15%3C2669::AID-HYP85%3E3.0.CO;2-Q)
- 749 Pfister, R., & Schneebeli, M. (1999). Snow accumulation on boards of different sizes and
750 shapes. *Hydrological Processes*, 13(14-15), 2345–2355. [https://doi.org/10.1002/\(SICI\)1099-9-1085\(199910\)13:14/15%3C2345::AID-HYP873%3E3.0.CO;2-N](https://doi.org/10.1002/(SICI)1099-9-1085(199910)13:14/15%3C2345::AID-HYP873%3E3.0.CO;2-N)
- 751 Pomeroy, J. W., Brown, T., Fang, X., Shook, K. R., Pradhananga, D., Armstrong, R., Harder,
752 P., Marsh, C., Costa, D., Krogh, S. A., Aubry-wake, C., Annand, H., Lawford, P., He,
753 Z., Kompanizare, M., & Moreno, J. I. L. (2022). The cold regions hydrological modelling
754 platform for hydrological diagnosis and prediction based on process understanding. *Journal
755 of Hydrology*, 615(128711), 1–25. <https://doi.org/10.1016/j.jhydrol.2022.128711>
- 756 Pomeroy, J. W., Fang, X., & Ellis, C. R. (2012). Sensitivity of snowmelt hydrology in Marmot
757

- 761 Creek, Alberta, to forest cover disturbance. *Hydrological Processes*, 26(12), 1891–1904.
762 <https://doi.org/10.1002/hyp.9248>
- 763 Pomeroy, J. W., Marsh, P., & Gray, D. M. (1997). Application of a distributed blowing snow
764 model to the arctic. *Hydrological Processes*, 11(11), 1451–1464. [https://doi.org/10.1002/\(SICI\)1099-1085\(199709\)11:11%3C1451::aid-hyp449%3E3.0.co;2-q](https://doi.org/10.1002/(SICI)1099-1085(199709)11:11%3C1451::aid-hyp449%3E3.0.co;2-q)
- 766 Pomeroy, J. W., Parviainen, J., Hedstrom, N., & Gray, D. M. (1998). Coupled modelling of
767 forest snow interception and sublimation. *Hydrological Processes*, 12(15), 2317–2337. [https://doi.org/10.1002/\(SICI\)1099-1085\(199812\)12:15%3C2317::AID-HYP799%3E3.0.CO;2-X](https://doi.org/10.1002/(SICI)1099-1085(199812)12:15%3C2317::AID-HYP799%3E3.0.CO;2-X)
- 769 Pomeroy, J. W., & Schmidt, R. A. (1993). The use of fractal geometry in modelling intercepted
770 snow accumulation and sublimation. *Eastern Snow Conference*, 50, 231–239.
- 771 R Core Team. (2024). *R: A language and environment for statistical computing* [Manual]. R
772 Foundation for Statistical Computing.
- 773 Rittger, K., Raleigh, M. S., Dozier, J., Hill, A. F., Lutz, J. A., & Painter, T. H. (2020). Canopy
774 adjustment and improved cloud detection for remotely sensed snow cover mapping. *Water
775 Resources Research*, 56(6), n/a. <https://doi.org/10.1029/2019WR024914>
- 776 Roesch, A., Wild, M., Gilgen, H., & Ohmura, A. (2001). A new snow cover fraction parame-
777 terization for the ECHAM4 GCM. *Climate Dynamics*, 17(12), 933–946. <https://doi.org/10.1007/s003820100153>
- 779 Roth, T. R., & Nolin, A. W. (2019). Characterizing maritime snow canopy interception in
780 forested mountains. *Water Resources Research*, 55(6), 4564–4581. <https://doi.org/10.1029/2018WR024089>
- 782 Safa, H., Krogh, S. A., Greenberg, J., Kostadinov, T. S., & Harpold, A. A. (2021). Unraveling
783 the controls on snow disappearance in montane conifer forests using multi-site lidar. *Water
784 Resources Research*, 57(12), 1–20. <https://doi.org/10.1029/2020WR027522>
- 785 Satterlund, D. R., & Haupt, H. F. (1967). Snow catch by conifer crowns. *Water Resources
786 Research*, 3(4), 1035–1039. <https://doi.org/10.1029/WR003i004p01035>
- 787 Schmidt, R. A., & Gluns, D. R. (1991). Snowfall interception on branches of three conifer
788 species. *Canadian Journal of Forest Research*, 21(8), 1262–1269. <https://doi.org/10.1139/x91-176>

- 790 Schmidt, R. A., & Troendle, C. A. (1989). Snowfall into a forest and clearing. *Journal of*
791 *Hydrology*, 110(3-4), 335–348. [https://doi.org/10.1016/0022-1694\(89\)90196-0](https://doi.org/10.1016/0022-1694(89)90196-0)
- 792 Smith, C. D. (2007). Correcting the wind bias in snowfall measurements made with a Geonor
793 T-200B precipitation gauge and alter wind shield. *87th AMS Annual Meeting*.
- 794 Staines, J., & Pomeroy, J. W. (2023). Influence of forest canopy structure and wind flow
795 on patterns of sub-canopy snow accumulation in montane needleleaf forests. *Hydrological*
796 *Processes*, 37(10), 1–19. <https://doi.org/10.1002/hyp.15005>
- 797 Storck, P., Lettenmaier, D. P., & Bolton, S. M. (2002). Measurement of snow interception and
798 canopy effects on snow accumulation and melt in a mountainous maritime climate, Oregon,
799 United States. *Water Resources Research*, 38(11), 1–16. <https://doi.org/10.1029/2002wr001281>
- 800 Troendle, C. A. (1983). The potential for water yield augmentation from forest management
801 in the rocky mountain region. *Journal of the American Water Resources Association*, 19(3),
802 359–373. <https://doi.org/10.1111/j.1752-1688.1983.tb04593.x>
- 803 Valante, F., David, J. S., & Gash, J. H. C. (1997). Modelling interception loss for two sparse
804 eucalypt and pine forests in central Portugal using reformulated Rutter and Gash analytical
805 models. *Journal of Hydrology*, 190(1-2), 141–162. [https://doi.org/10.1016/S0022-1694\(96\)03066-1](https://doi.org/10.1016/S0022-1694(96)03066-1)
- 806 Van Stan, J. T., Siegert, C. M., Levia, D. F., & Scheick, C. E. (2011). Effects of wind-
807 driven rainfall on stemflow generation between codominant tree species with differing crown
808 characteristics. *Agricultural and Forest Meteorology*, 151(9), 1277–1286. <https://doi.org/10.1016/j.agrformet.2011.05.008>
- 809 Varhola, A., Coops, N. C., Weiler, M., & Moore, R. D. (2010). Forest canopy effects on
810 snow accumulation and ablation: An integrative review of empirical results. *Journal of*
811 *Hydrology*, 392(3-4), 219–233. <https://doi.org/10.1016/j.jhydrol.2010.08.009>
- 812 Vionnet, V., Mortimer, C., Brady, M., Arnal, L., & Brown, R. (2021). Canadian historical
813 snow water equivalent dataset (CanSWE, 1928–2020). *Earth System Science Data*, 13(9),
814 4603–4619. <https://doi.org/10.5194/essd-13-4603-2021>
- 815 Watanabe, S., & Ozeki, J. (1964). Study of fallen snow on forest trees (II). Experiment on the

- 819 snow crown of the Japanese cedar. *Jap. Govt. Forest Exp. Sta. Bull*, 169, 121–140.
- 820 Wheeler, K. (1987). Interception and redistribution of snow in a subalpine forest on a storm-
- 821 by-storm basis. In *55th annual western snow conference*. Western Snow Conference.